Supplementary Information (SI) for Energy & Environmental Science.

Boosting Interfacial Zn^{2+} Desolvation Kinetics by a π-Electron-Rich Janus Catalyst for Robust Zinc Metal Batteries

Yinze Zuo[a,b], Zheng Wang[a,b], Mingquan Liu[a,b] *, Linlong Lu[a,b], Yidong Jiang[a,b], Jie Lei[a,b], Hao Yan[a,b], Hongwei Li[a,b], Wei Yan[a,b] *, Jiujun Zhang[a,b] *

[a]College of Materials Science and Engineering, Fuzhou University, Fuzhou 350108, China

[b]Fujian Engineering Research Center of High Energy Batteries and New Energy Equipment & Systems, Fuzhou University, Fuzhou, 350108, China

E-mail: liumingquan@fzu.edu.cn; weiyan@fzu.edu.cn; jiujun.zhang@fzu.edu.cn

Experimental Section

Preparation of COP and COP@Zn electrode: The two-dimensional layered covalent organic polymer (COP) was fabricated via a hydrothermal reaction. Firstly, 378 mg of melamine and 670 mg of p-phthalaldehyde were added into 80 mL 1,4-dioxane/mesitylene (v/v = 1:1) mixed solution under stirring for 10 minutes, then 5 mL 6 M acetic acid was introduced with stirring for 60 minutes to form a mixed solution. This mixed solution was heated at 210 °C for 24 hours. After cooling down to the room temperature, the COP was collected by centrifugation and washing with 1,4-dioxane, tetrahydrofuran and acetone, and followed by drying at 80 °C for 6 hours in a vacuum oven. The obtained COP powder was further exfoliated in acetone by sonicating for 3 hours to produce the COP nanosheets. The COP-coated Zn (COP@Zn) was prepared by mixing PVDF and COP (1:9) in proper amount of NMP solvent by well grinding, followed by blade-coating the slurry onto Zn foil, which was dried in vacuum at 60℃ overnight.

Preparation of KVO powders and KVO electrodes: 365 mg V_2O_5 was dissolved in 50 mL DI water containing 2 mL H_2O_2 (30%) to form Solution A. Solution B was composed of K_2SO_4 and V_2O_5 with a molar ratio of 1:4 dissolved in 30 mL DI water. Then, the above two solutions were mixed under stirring for 0.5 hour and transferred into Teflon lined stainless steel autoclave under 120 ℃ for 6 hours. Finally, the KVO powder was obtained by centrifugation and washing with DI water and ethanol for three times and dried in an oven at 60 ˚C overnight. The KVO electrode was fabricated by blade-coating the slurry containing KVO, Super P, PVDF (8:1:1) in NMP onto the Ti foil, followed by a drying under vacuum at 80 °C for 12 hours. The mass loadings of the electrodes for the coin cell and pouch cell (4.9 cm × 5 cm) are ~2 mg cm^{-2} and ~5.46 mg cm^{-2}, respectively.

Electrochemical Measurements: Electrochemical performances were evaluated by symmetric cells assembled by two identical Zn (100 μm) or COP@Zn plates, glass fiber separator (GF/D), and 2 M $ZnSO_4$ aqueous solution using 2032 coin-type cells. The Zn//Cu asymmetric cells were constructed to investigate the Zn plating/stripping Coulombic efficiency. The cycling performance and rate capability of the Zn symmetric cell and Zn//KVO full cell are tested on a LAND-CT3002A battery-testing instrument. The pouch cells were assembled by a large-sized Zn anode and a high-mass-loading cathode (5 × 4.9 cm^2, 5.5 mg cm^{-2} for the cathode). The separator (GF/B, Whatman) was slightly larger than the electrodes to prevent direct contact. During electrochemical testing, the pouch cell was clamped with acrylic sheets and fixed with dovetail clips to prevent poor contact between the cathode and anode. The linear polarization curve (LSV) and Tafel corrosion tests were performed to investigate the anti-corrosion stability of the Zn anode. LSV was conducted in a three-electrode configuration in 2 M Na_2SO_4 aqueous electrolyte, where bare Zn or COP@Zn serves as the working electrode, Pt foil serves as the counter electrode, and Ag/AgCl serves as the reference electrode. Chronoamperometry (CA) and electrochemical impedance spectroscopy (EIS, frequency range from 0.01 Hz to 100 kHz) were conducted to investigate the interfacial dynamical kinetics and interfacial resistance. Cyclic voltammetry of the full cell was carried out at a voltage range of 0.2−1.6 V. The galvanostatic intermittent titration technique (GITT) were executed on LAND-CT3002A battery testing system with a voltage range of 0.2 to 1.6 V. A constant current density (0.1 A g^{-1}) was applied to the cell for 120 seconds followed by 10 minutes of open-circuit relaxation, and the steps were repeated until the voltage reached 0.2 V or 1.6 V.

Material characterization:

The microstructures of the Zn metals during corrosion testing and plating/stripping were investigated by scanning electron microscope (SEM, Hitachi S-4800). The crystal phase structures of the Zn anodes were characterized by X-ray diffraction (Bruker AXS, Karlsruhe, Germany). The microstructure of the COP layer was studied by high-resolution transmission electron microscopy (HRTEM, JEOL TEM-2010) and SEM. The composition of the COP and the chemical information of the Zn surface were investigated by X-ray photoelectron spectra (XPS, PHI5700). The interfacial properties of the Zn anodes during Zn plating/stripping were studied by in-situ Raman spectroscopy (WITec GmbH, Ulm, Germany) and in-situ Fourier transform infrared spectrometer (FTIR, Nicole iS50). The real-time deposition of Zn^{2+} was performed by the operando optical microscope (LIB-MS-II). The surface composition of the Zn anode was also investigated by time-of-flight secondary ion mass spectrometry (TOF-SIMS, Scios 2 Hivac, Thermo scientific) equipped with a 30 keV Ga ion sputter gun.

In-situ measurements:

In-situ Raman spectroscopy. Zn//Zn (COP@Zn//COP@Zn) transparent electrochemical cells (LIB-MS-II, Beijing Scistar Technology Co., Ltd.) were used for the in-situ Raman spectroscopy analysis at 532 nm Laser. The laser shines through the quartz window to the side of the Zn deposit for Raman signal collection. The cells were tested at a rate of 1 mA cm^{-2}.

In-situ digital camera. The in-situ characterization of Zn plating behavior on the Zn and COP@Zn in 2 M $ZnSO_4$ aqueous electrolyte was performed on an optical microscope (YM700, YM710R) equipped with a digital camera and the plating current density was 5.0 mA cm^{-2} for 40 minutes. The in-situ cell was assembled by in-situ in transparent electrochemical cell (LIB-MS-II, Beijing Scistar Technology Co., Ltd.)

In-situ fourier transform infrared spectroscopy (FTIR). The in-situ FTIR was performed by Thermo Scientific Nicolet iS50 spectrometer system with a liquid N_2-cooled MCT-A detector in a customized cell from Beijing Scistar Technology Co. Ltd. In the in-situ FTIR cell, the Zn(COP@Zn) foil was used as the working electrode and Zn foil was the counter and reference electrodes, respectively. Zn was plated at 1 mA for 60 minutes with 2 M $ZnSO_4$. Note that the background was first collected in the atmosphere, then the first spectrum after filling the electrolyte (A(t0)), and the second spectrum ($A(t_2)$, under current load, within the time resolution of IR), as well as subsequent spectra ($A(t_x)$) were collected.

In-situ electrochemical impedance spectroscopy (EIS). Operando EIS was performed for Zn//Zn symmetric cells during Zn deposition in Autolab M204. EIS was taken from 100 kHz to 0.1 Hz with an amplitude of 10 mV after constant-current step and following rest. The Zn plating current density was 1 mA cm^{-2}. Distribution relaxation times (DRT) from EIS data were calculated by MatlabR2021 with a toolbox of DRT-TOOLS developed by the research group of Professor Francesco Ciucci1 (DRT-TOOLS), which is freely available under the GNU license from the following site: (https://sites.google.com/site/drttools/)[1].

Density Functional Theory (DFT) Calculations

In this work, the DFT calculations with periodic models were performed by the Vienna Ab initio Simulation Package (VASP) [2, 3]. A generalized gradient approximation (GGA) [4] with projector augmented wave (PAW) [5] method was applied in calculations to better simulate the electronic structures and the core-electron interaction. The cutoff energy for all the computations was set 450 eV, and the force threshold of optimization convergence was 0.05 eV $Å^{-1}$. To calculate the adsorption energies of the obtained molecules on the considered slab, the following formula was used:

$$E_{ads} = E_{slab + molec} - E_{slab} - E_{molec} \tag{S1}$$

where $E_{slab + molec}$ means the total energy of the slab with species adsorbed, E_{slab} indicates the energy of the slab, and E_{molec} represents the energy of the molecule in vacuum.

Charge density difference analysis was employed in this work to study the charge transfer during species adsorption. In this scenario, the following formula was used:

$$\Delta\rho = \rho_{a + b} - \rho_a - \rho_b \tag{S2}$$

where $\rho_{a + b}$ indicates the overall charge density of the system containing a and b, ρ_a or ρ_b represents the charge density of system a or b.

The successive desolvation energy under different model adsorption conditions ($E_{d\text{-}slab}$):

$$E_{d - slab} = E_{\left[Zn\left(H_2O\right)_{n - 1}\right]^{2 +}/slab} + E_{H_2O} - E_{\left[Zn\left(H_2O\right)_n\right]^{2 +}/slab} \tag{S3}$$

where $E_{\left[Zn\left(H_2O\right)_{n - 1}\right]^{2 +}/slab}$ means the total energy of $[Zn(H_2O)_{n-1}]^{2+}$ on different slab surface, E_{H_2O} indicates the energy of H_2O on different slab surface, and $E_{\left[Zn\left(H_2O\right)_n\right]^{2 +}/slab}$ represents the energy of $[Zn(H_2O)_n]^{2+}$ on different slab surface. In addition, the counterions and the second solvation shell were ignored.

Molecular Dynamic (MD) Simulations

The MD simulations were conducted by the Forcite module in Materials Studio to explore influence of COP material on the Zn^{2+} solvation structure comprising 1665 water molecules, 60 $ZnSO_4$ units on the Zn and COP@Zn surface. Moreover, the COMPASS II force field of Forcite module was used within the simulation system. First, the geometry optimization algorithm was used with a combination of the steepest descent, adopting basis Newton-Raphson, and quasi-Newton methods based on the convergence of the total energy (0.0001 kcal mol^{-1}) with a force of 0.05 kcal mol^{-1} $Å^{-1}$. After geometric optimization, the NPT (250 s) was performed to optimize the density of the solution under a pressure of 0.1 MPa and a constant temperature of 298 K. The final configurations from the simulations were subject to additional equilibration simulations under NVT ensemble (T = 298 K) for a 500 ps. Forcite analysis was used to calculate the radial distribution function (RDF) of Zn^{2+} solvation structure.

Quantum Chemical Calculations

All calculations were performed using Gaussian16 software. Here, we used the B3LYP density functional with Grimme's empirical dispersion correction and BJ-damping (D3(BJ)). All geometric configurations were used 6-311++G (d,p) basis sets for C, H, N, O atoms and the SDD basis sets for Zn. The NBO calculation was performed using the NBO program that implemented with Guassian16. Analyses of PI population and PI electron density isosurface were performed with the Multiwfn 3.8 and VMD programs. All geometries were prepared using CYLView software and VMD programs.

Finite Element Simulations

Finite element method (FEM) with Deformed Geometry Interface is employed to investigate the distribution of Zn ion concentration and electric potential by controlling ion and electron transport processes, based on COMSOL Multiphysics 6.1 platform. Electrochemical reactions were driven by the Butler-Volmer equation. A two-dimensional domain with a size of 20.0 μm × 20.0 μm was introduced. Pure Zn model included electrolyte and Zn nucleation sites, POMDOL layer model included electrolyte, coating layer and Zn nucleation sites. A constant current density of 5 mA cm^{-2} was applied in these galvanostatic models. The diffusion coefficient of Zn ions within electrolyte and coating layer was set as 3.68×10^{-10} m^2 s^{-1}. The initial concentration of Zn ions and upper boundary concentration were set as 2.0 M.

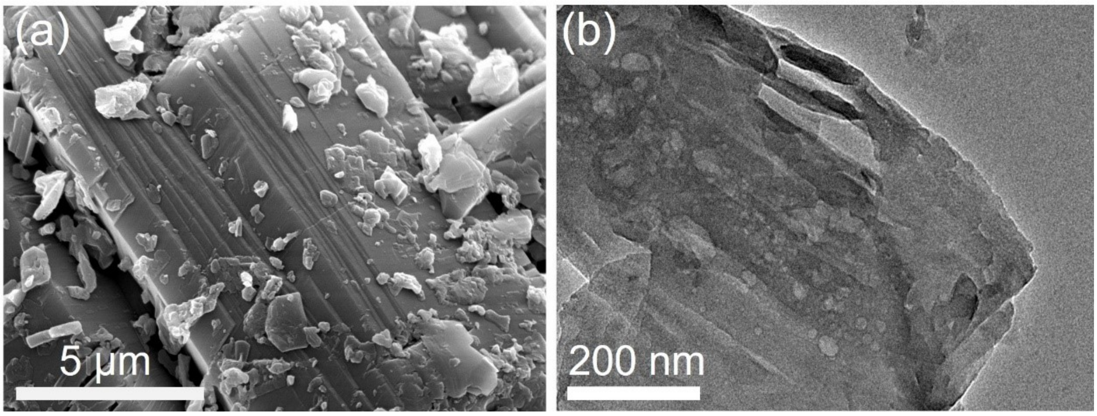

Figure S1. (a) SEM image of the pristine COP. (b) TEM image of the pristine COP.

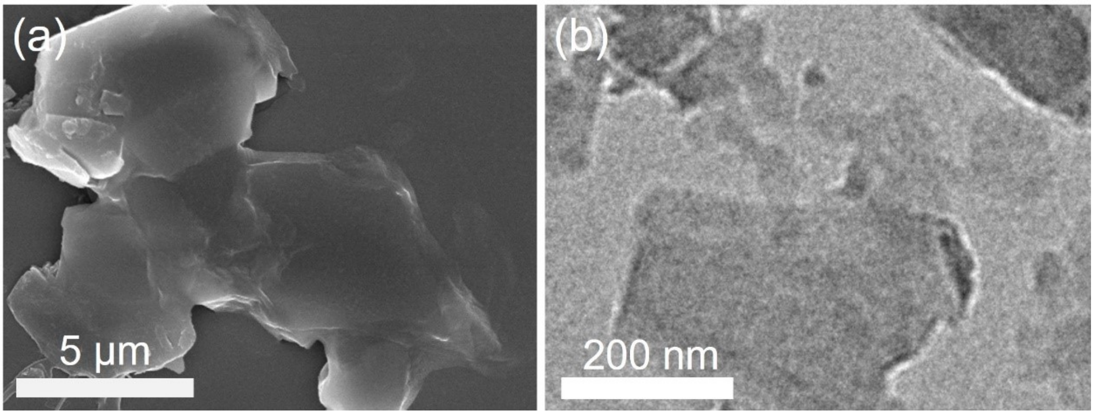

Figure S2. (a) SEM image and (b) TEM image of the exfoliated layered COP.

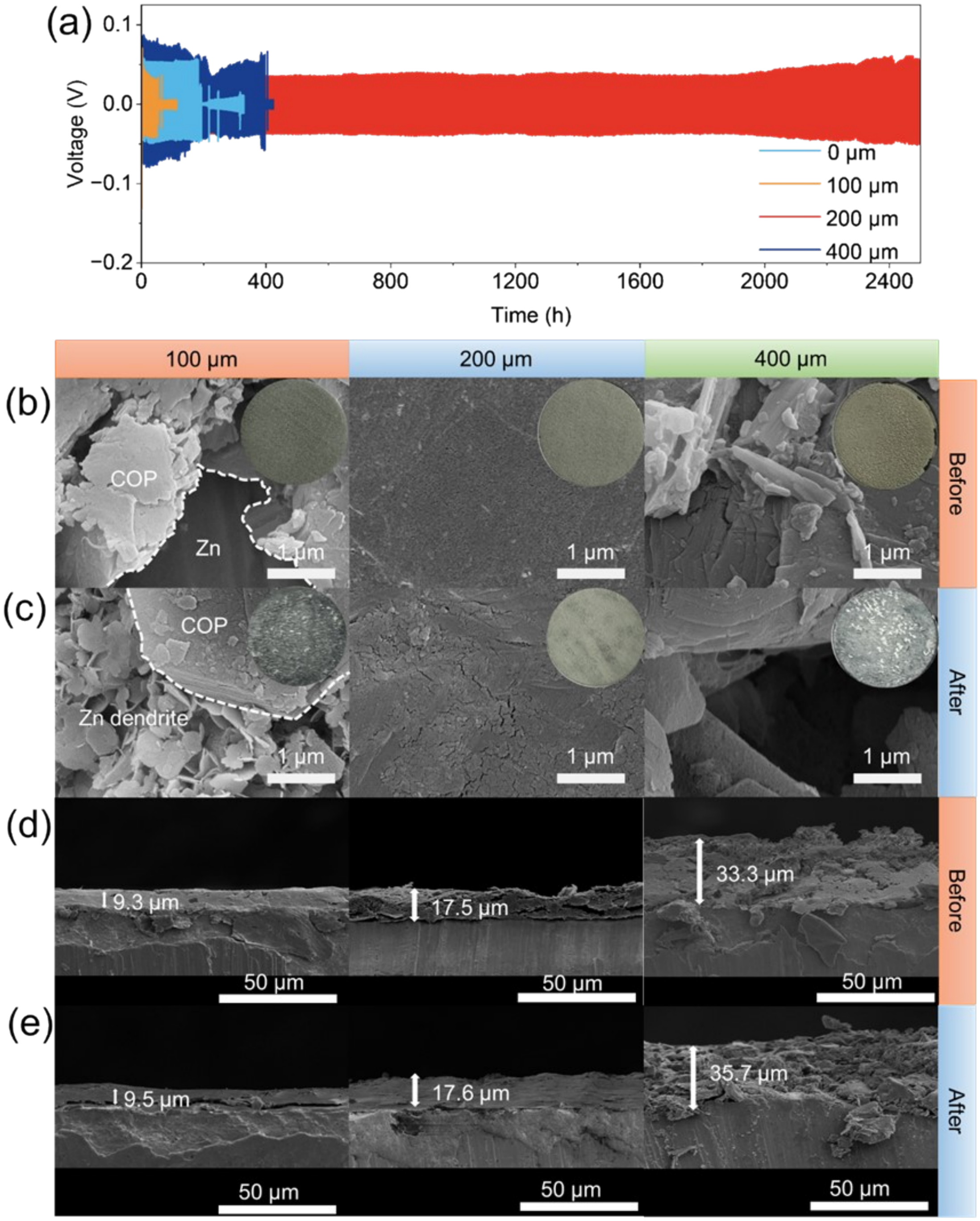

Figure S3. (a) Cycling stability of the Zn//Zn symmetric cells at 1 mA cm^{-2}/1 mAh cm^{-2} under varying COP thicknesses. SEM images of the COP@Zn anode using different blade coating thicknesses (b) before and (c) after Zn deposition. The front views of the COP@Zn anodes with different COP coating thicknesses (d) before and (e) after Zn deposition at 1 mA cm^{-2} for 2 h.

To obtain the optimal thickness of the COP coating, the long-term cycling performances of the Zn-based symmetric cells with different COP coating thicknesses by controlling the blade coating thicknesses (100, 200, 400 μm) have been conducted.

As shown in Figure S3a, the COP@Zn anode using 200 μm-thick blade coating displays the best cycling lifespan of 2500 h at 1 mA cm^{-2}/1 mAh cm^{-2}. It can be obtained that the voltage hysteresis is decreased for the COP@Zn anode using 100 and 200 μm-thick blade coatings compared to the bare Zn anode (0 μm), which should be due to the enhanced desolvation and deposition kinetics by the COP layer. The initially decreased cycling lifespan for the COP@Zn anode using 100-μm blade coating compared to the bare Zn is ascribed to the more chaotic and nonuniform Zn deposition flux. As evidenced by SEM measurement, the 100-μm blade coating cannot completely cover the Zn surface, which contrarily leads to the uneven Zn deposition and dendrite formation. Moreover, such an incomplete coating causes the insufficient accommodating volume change during Zn plating. As shown in Figure S3, after Zn deposition at 1 mA cm^{-2} for 2 h, significant cracks are occurred between the COP layer and the Zn surface, confirming the insufficient inhibition effect on Zn dendrite growth. For the COP@Zn anode using 400-μm blade coating, the voltage hysteresis significantly enlarges and the cycling lifespan is also limited. It is because too thick insulate coating layer results in the larger electronic and ionic transport barrier. Moreover, too thick COP layer is not firmly attached to the Zn substrate, resulting in the cracks and detachment of the COP powers from the Zn surface. The cluttered COP layer further leads to the nonuniform Zn deposition. By contrast, the optimal 200-μm blade coating contributes to the appropriate COP coating for both efficient electronic/ionic transport and the ability to accommodate volume change during Zn deposition, as confirmed by complete and smooth coverage on the Zn surface, as well as the firmly adhered of the COP layer on the Zn substrate even after Zn deposition. The above discussion proves that the COP layer using 200-μm blade coating is the optimal condition.

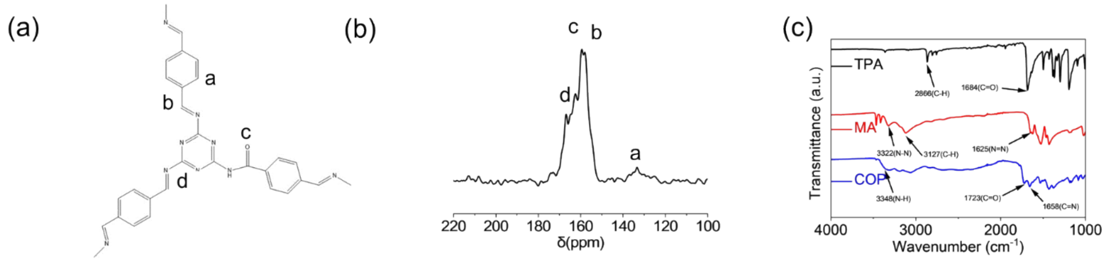

Figure S4. (a) Molecule structure of the COP. (b) Solid-state ^{13}C NMR spectra of the COP. (c) FTIR spectra of the COP.

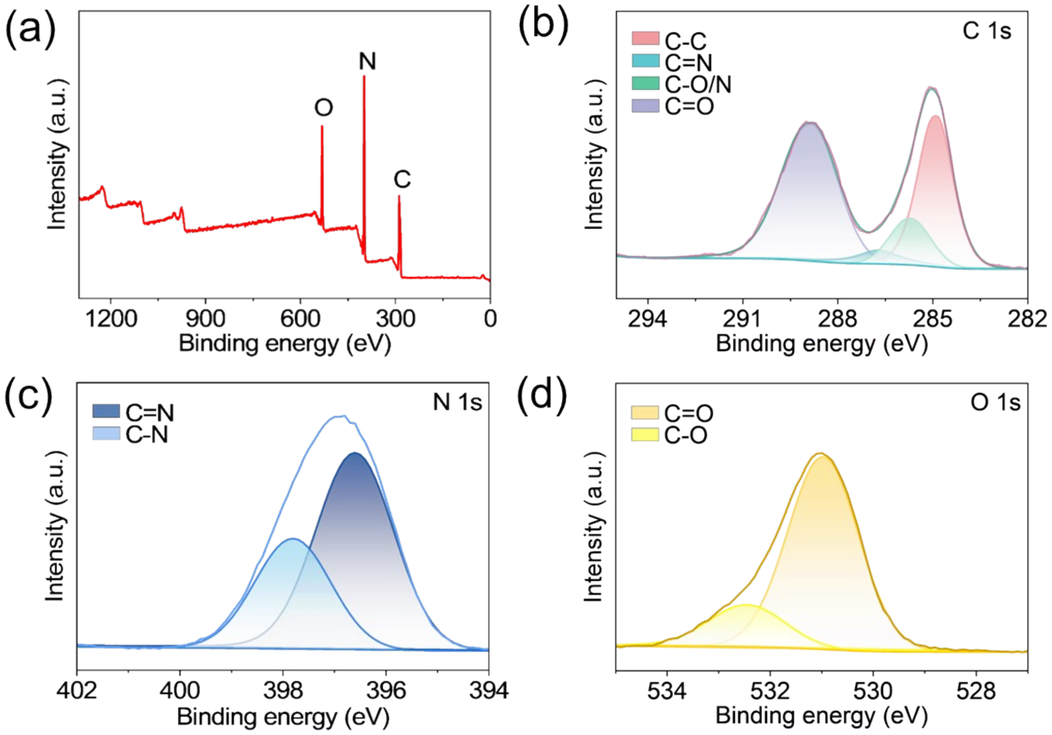

Figure S5. (a) Total XPS spectrum of the COP. High-resolution spectra of (b) C 1s, (c) N 1s and (d) O 1s of the COP.

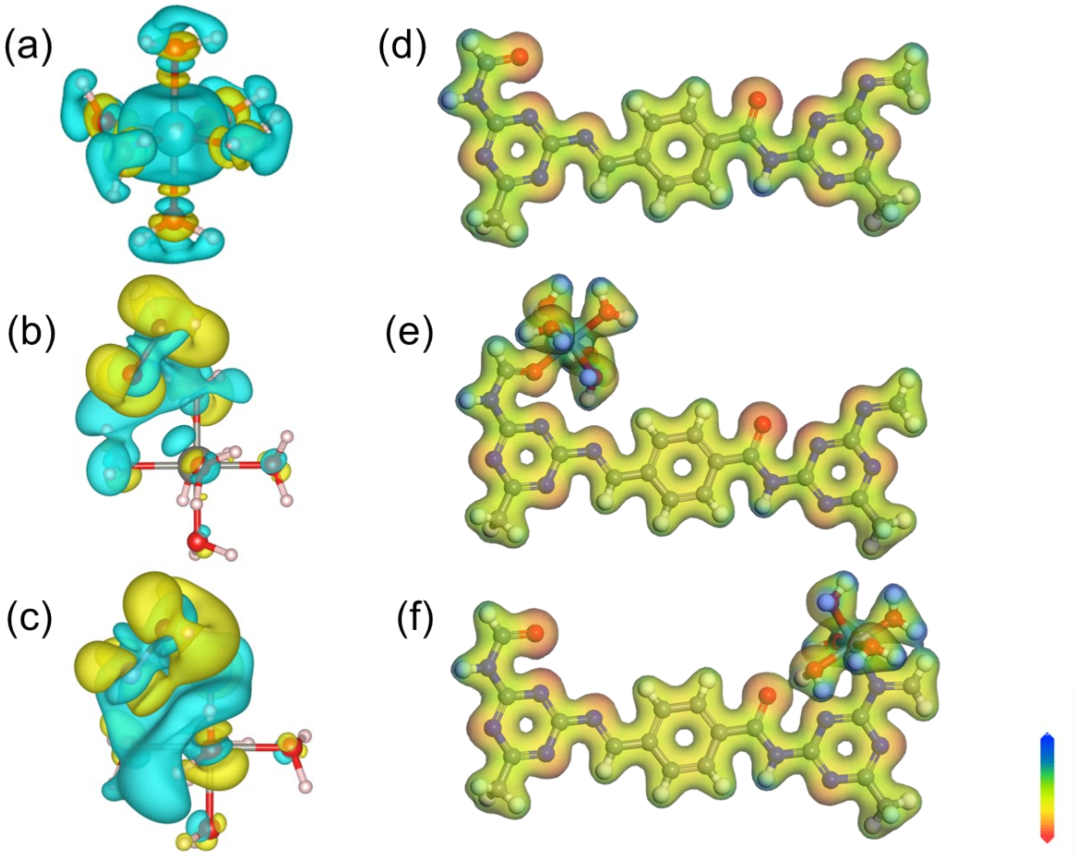

Figure S6. (a) The charge density difference of $[Zn(H_2O)_6]^{2+}$, (b, c) Charge density difference of $[Zn(H_2O)_6]^{2+}$ adsorbed on C=O and C=N active sites, (d-f) the electrostatic potential (ESP) distribution of one COF monomer, the Zn^{2+} of $[Zn(H_2O)_5]^{2+}$ adsorbed on different C=O and C=N active sites.

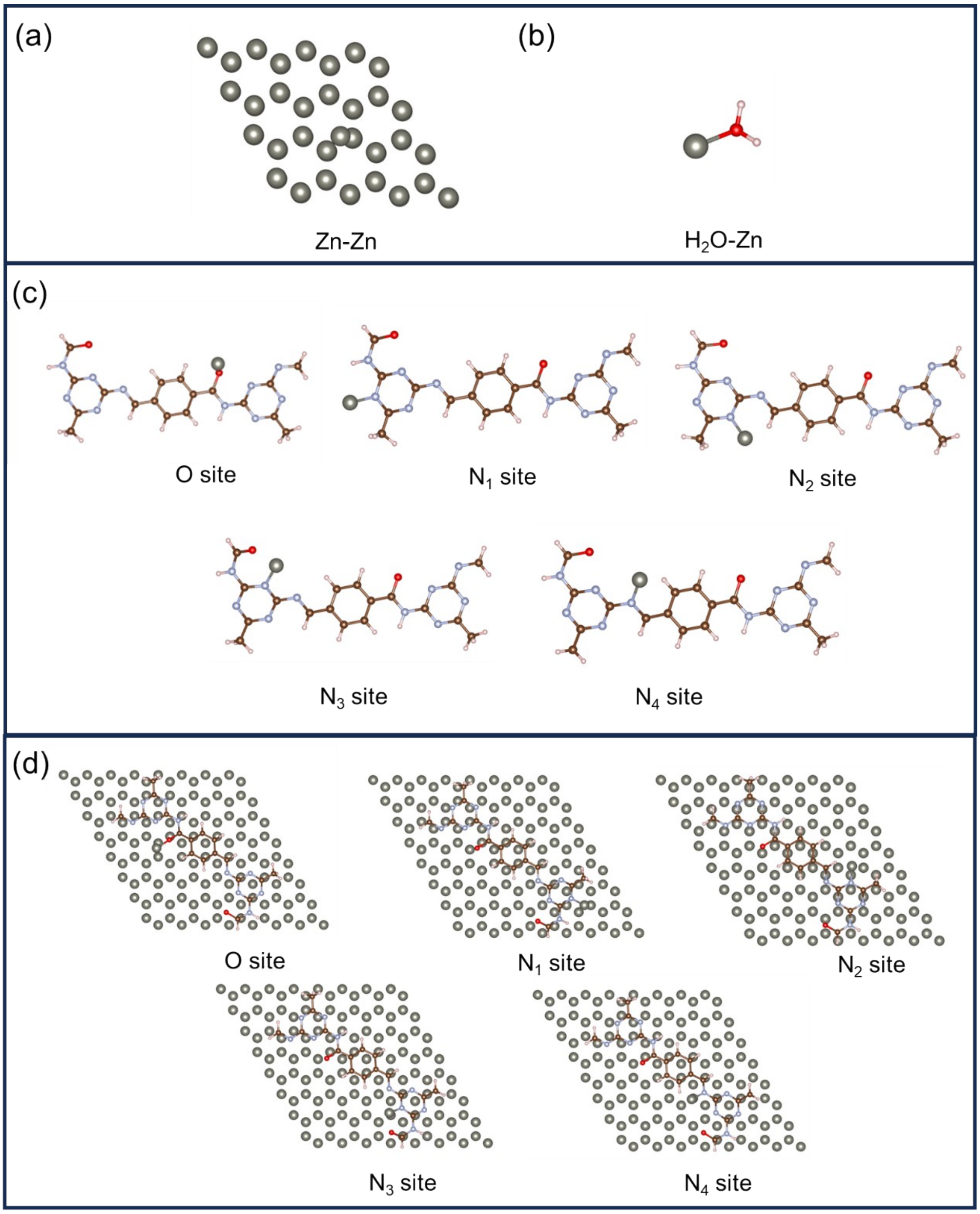

Figure S7. The calculation configurations of (a) Zn^{2+} adsorbed on the Zn metal, (b) Zn^{2+} adsorption by a H_2O molecule, (c) Zn^{2+} adsorption at C=O and different C=N sites in the COP without a Zn substrate, (d) Zn^{2+} adsorption at C=O and different C=N sites in the COP@Zn (COP was placed parallel to the Zn surface).

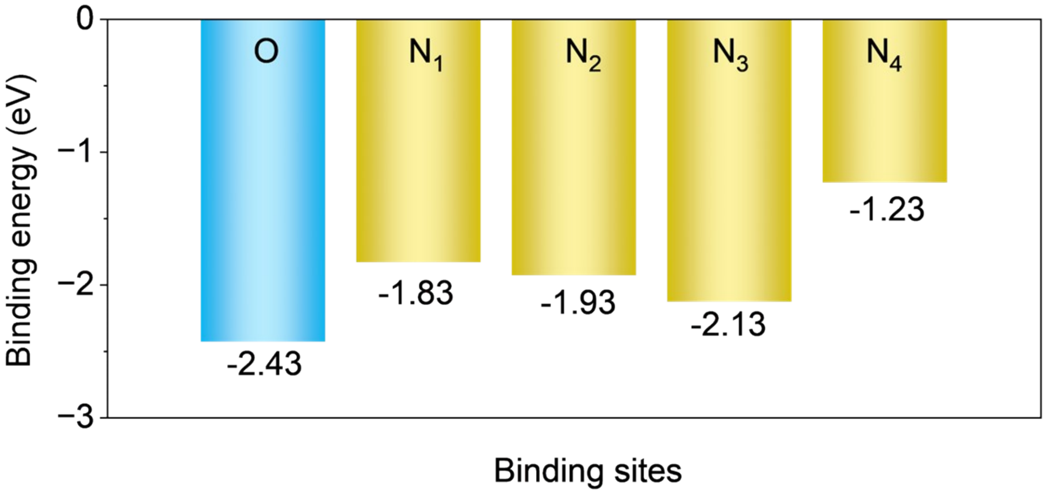

Figure S8. The Zn^{2+} adsorption energies at C=O and different C=N sites in the COP without a Zn substrate.

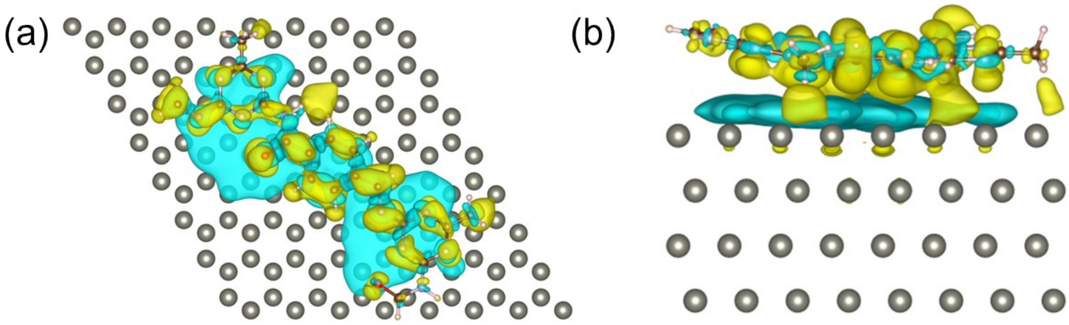

Figure S9. Charge density difference of the COP attached onto the Zn surface.

Figure S7c, d display the calculation models of Zn^{2+} adsorption at different sites in the COP with/without a Zn substrate. Notably, under both conditions, the Zn^{2+} adsorption energies (**Figure S8**, **Figure 1d**) at all C=N and C=O sites are higher than those at the bare Zn metal and the surrounding H_2O molecules, indicating that Zn^{2+} could be easily deposited at C=O/C=N sites of the COP layer. Moreover, according to the charge density difference of the COP attached onto the Zn surface (**Figure S9**), the electrons more likely transfer from Zn surface to the COP layer, resulting in electron enrichment on the COP to enhance the Zn^{2+} adsorption affinity of the COP layer.

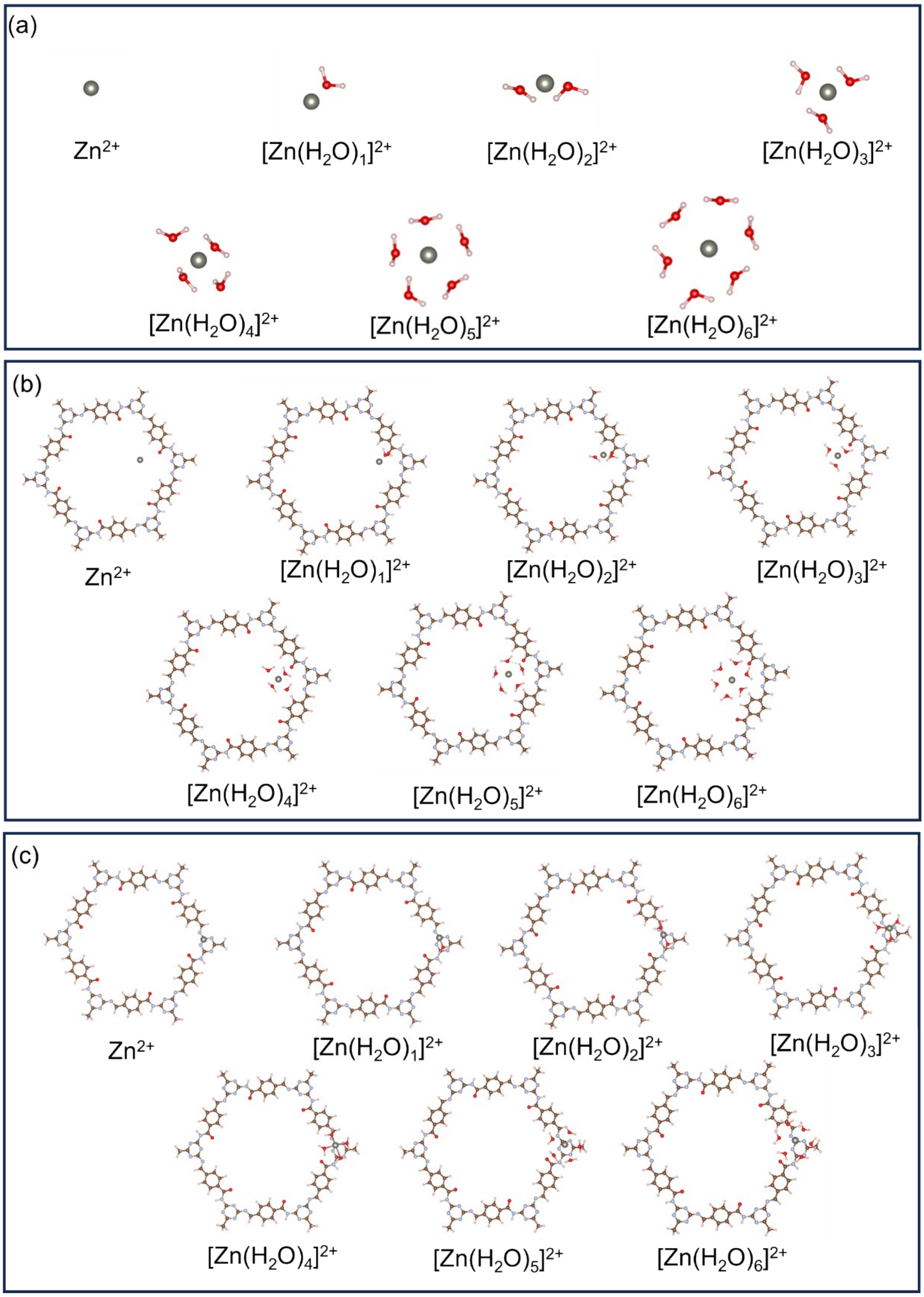

Figure S10. Molecular configuration (a) without and with COP around (b) O site or (c) N site in the process of Zn^{2+} desolvation.

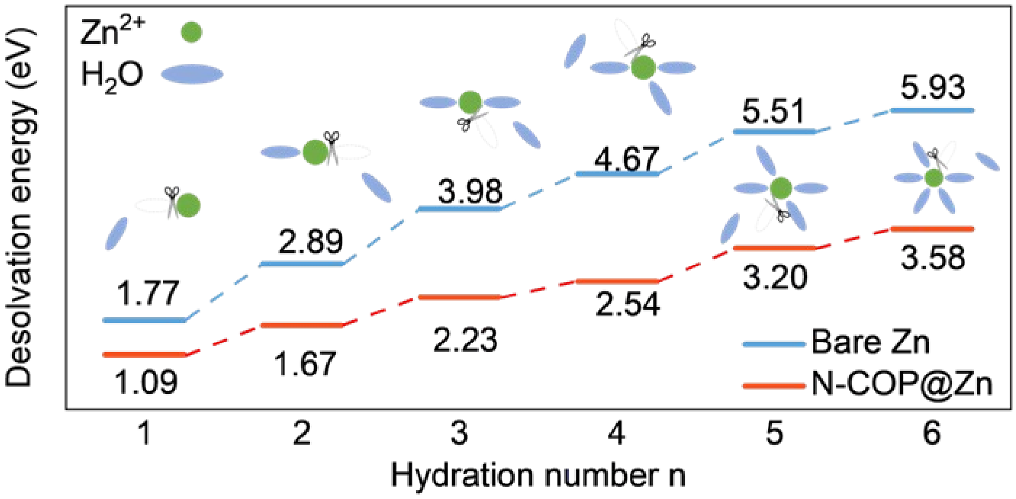

Figure S11. Comparison of energy barriers during the step-by-step desolvation process of $[Zn(H_2O)_6]^{2+}$ on the bare Zn and the C=N sites on the COP@Zn.

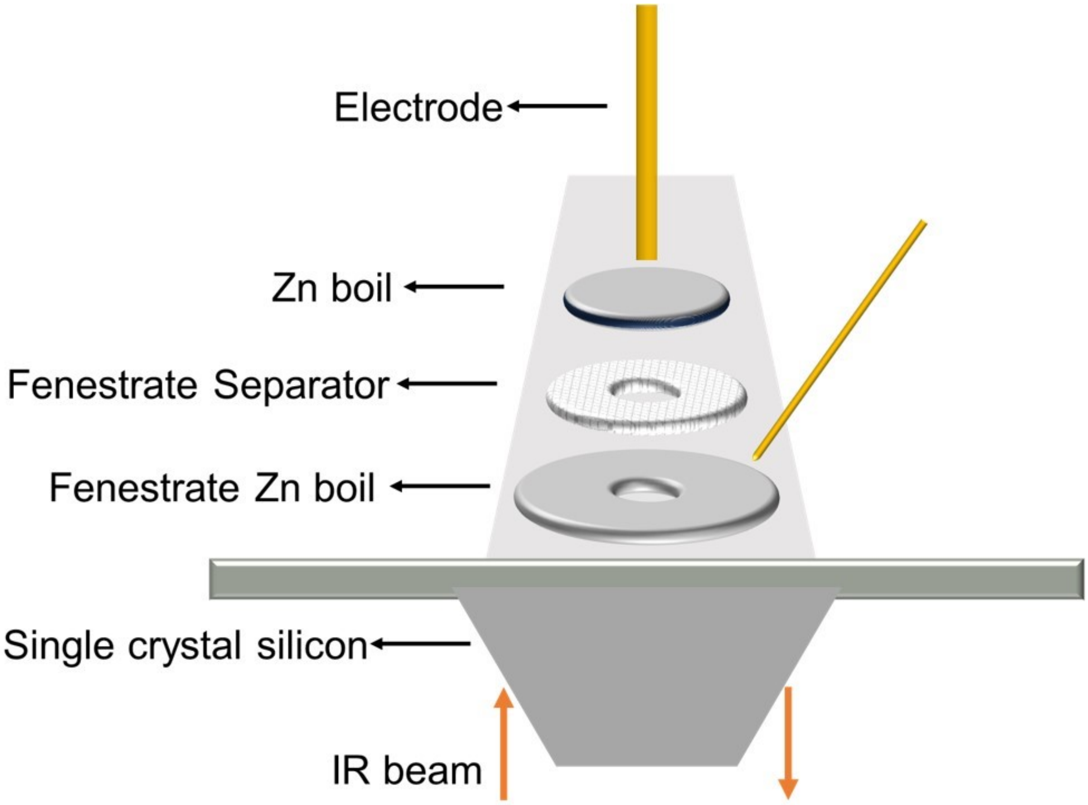

Figure S12. The device schematic of in-situ FTIR.

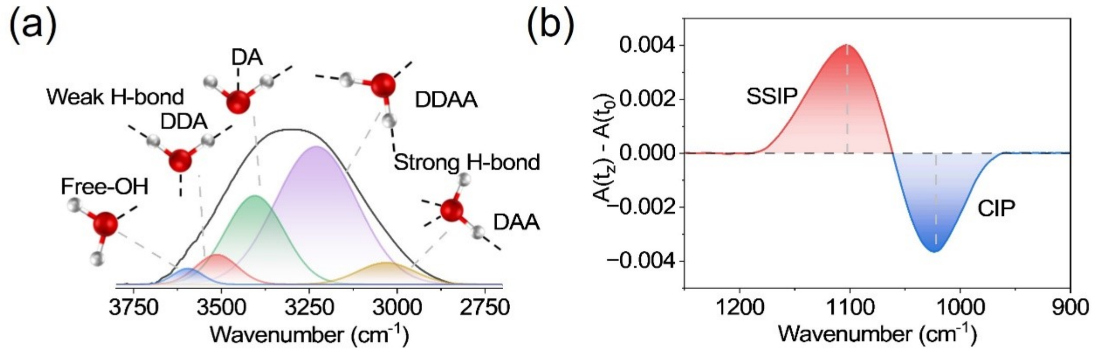

Figure S13. (a) The schematic of the local weak hydrogen-bond and strong hydrogen-bond. (b) The relative absorbance [A(t_x)-A(t_0)] of the SSIP and CIP.

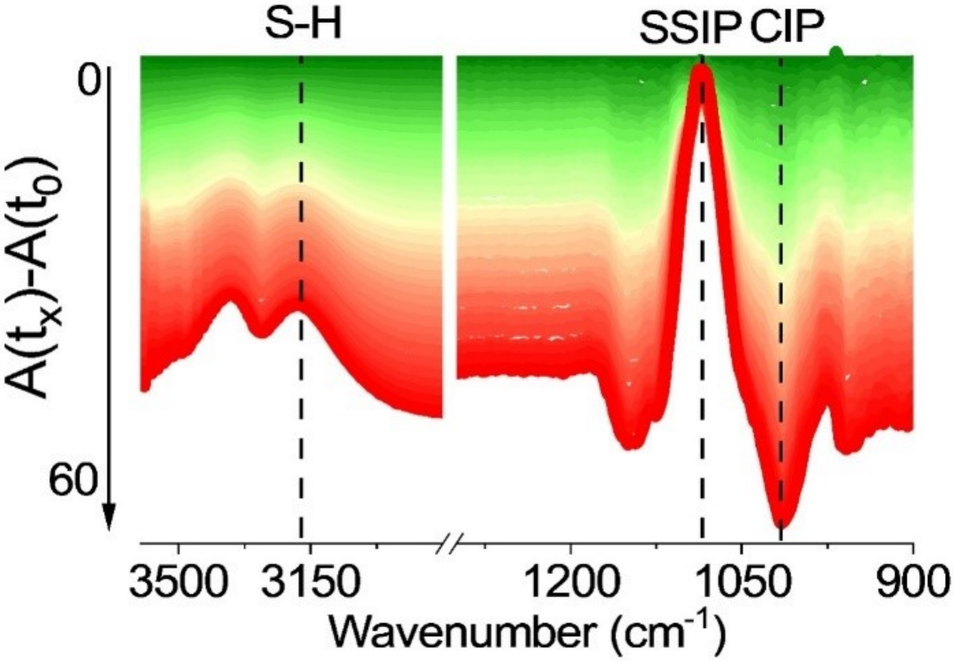

Figure S14. Evolution of the relative absorbance A(t_x)-A(t_0) during Zn plating based on the bare Zn anode.

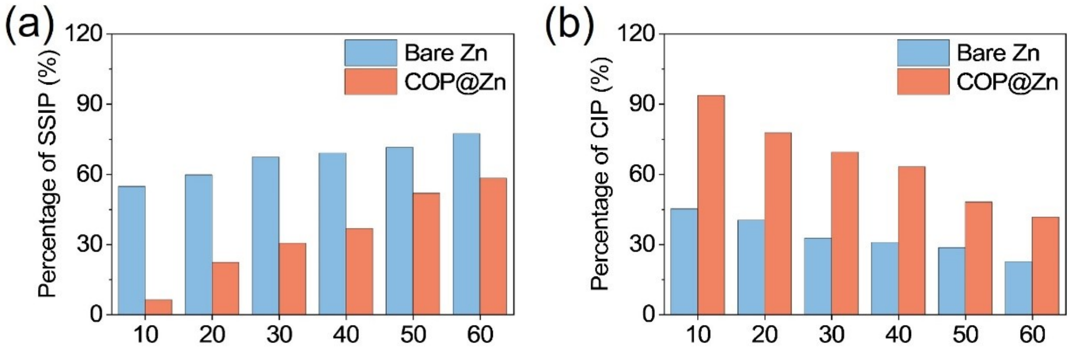

Figure S15. Comparison of (a) SSIP and (b) CIP contents before and after Zn deposition of in situ FTIR on bare Zn and COF@Zn anode.

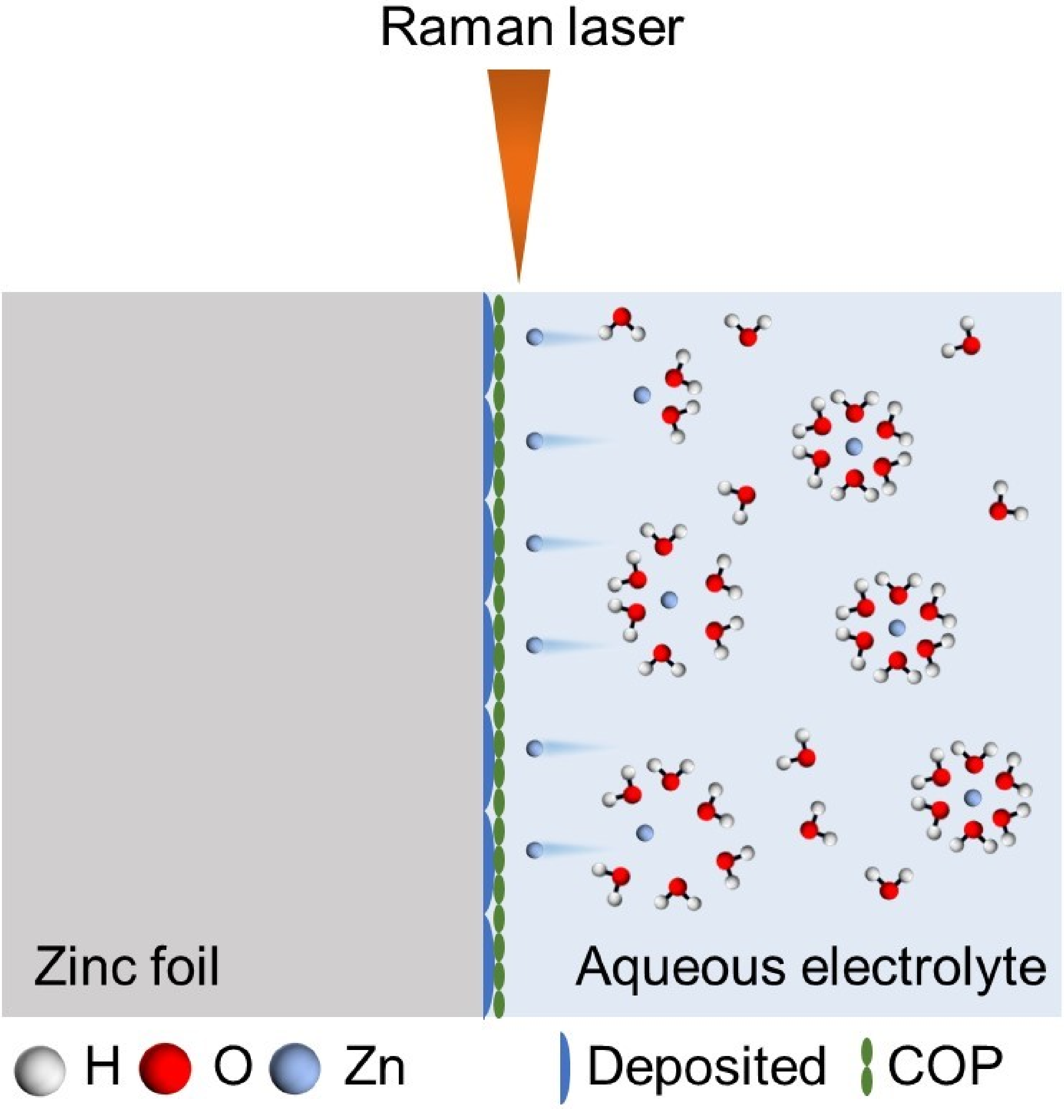

Figure S16. The device schematic of in-situ Raman spectroscopy.

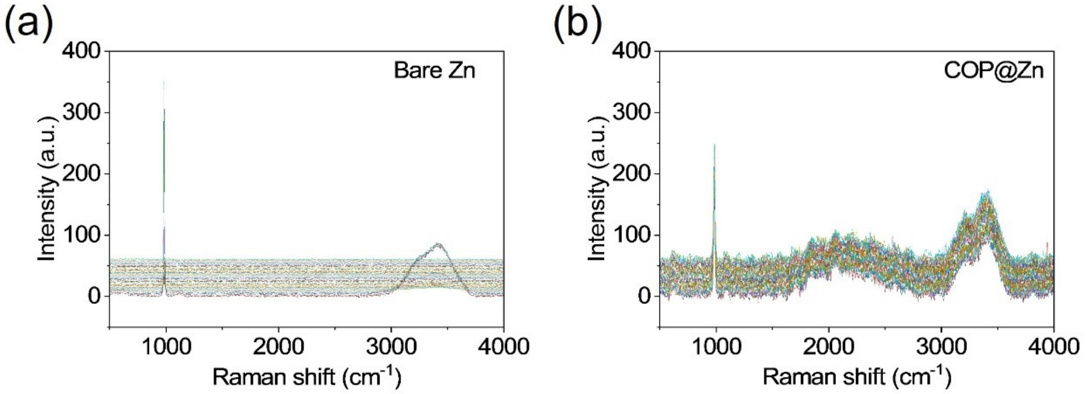

Figure S17. In situ Raman spectra collected during Zn plating in the Zn//Zn symmetric cell based on (a) bare Zn and (b) COP@Zn anodes.

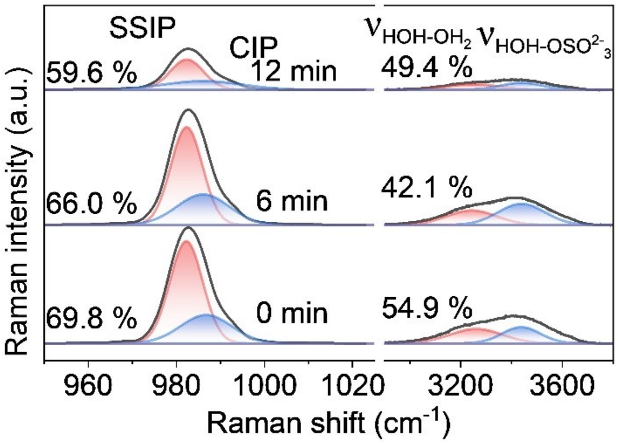

Figure S18. Evolution of the solvation structure according to ν-SO_4^{2-} band and O–H stretch vibration tested by in situ Raman during Zn plating on the bare Zn anode.

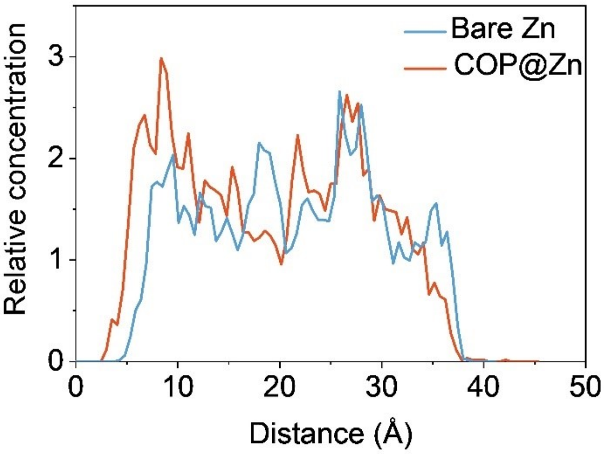

Figure S19. The Zn^{2+} concentration profile of the electrolytes near the bare Zn and the COP@Zn surface.

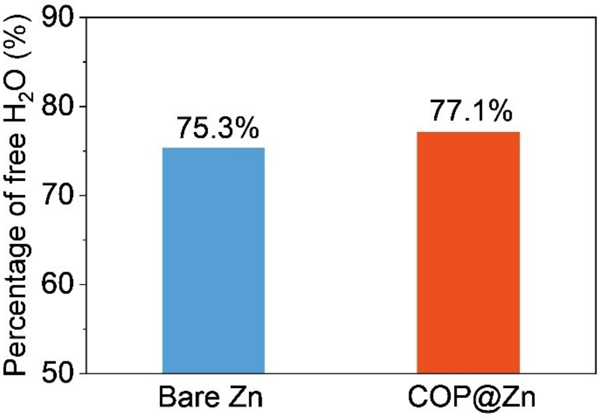

Figure S20. The percentage of free H_2O molecules in the electrolytes near the bare Zn and COP@Zn surfaces.

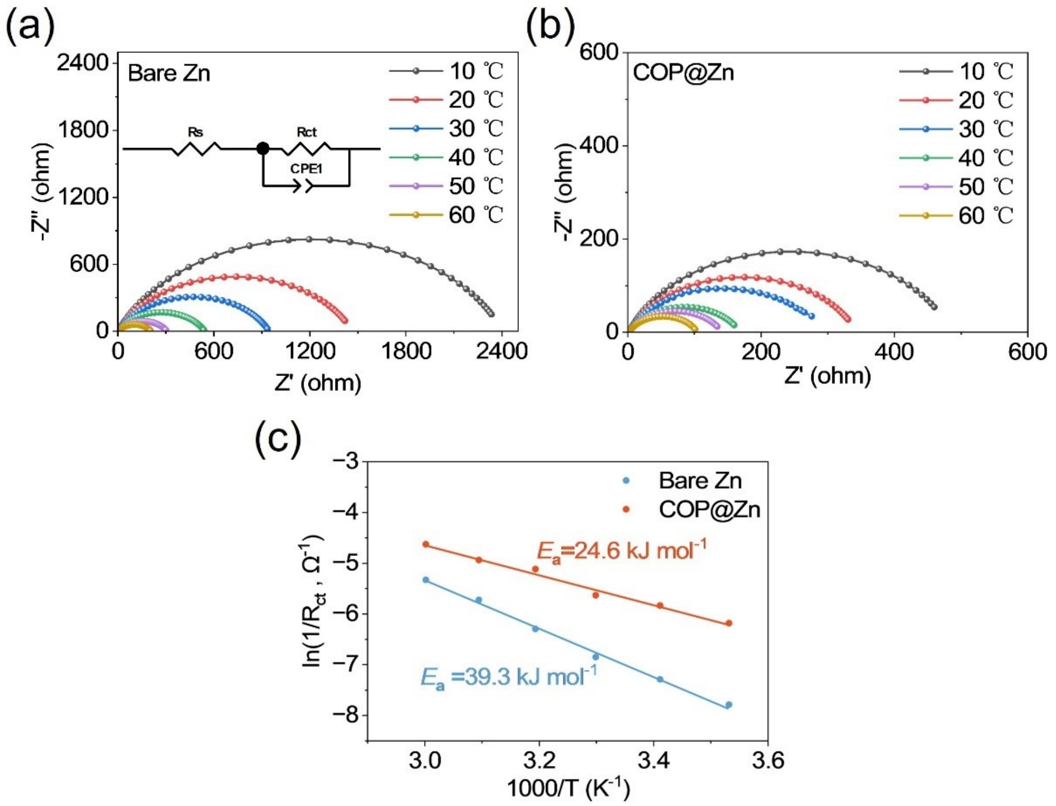

Figure S21. EIS curves at different temperatures of the Zn//Zn symmetric cells based on (a) the bare Zn anode and (b) the COP@Zn anode, and (c) the corresponding desolvation activation energies.

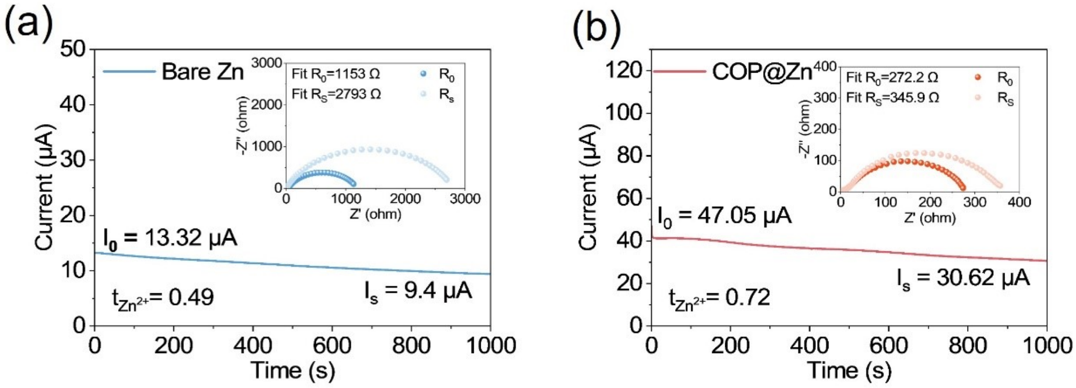

Figure S22. EIS curves of the Zn//Zn symmetric cells before and after the CA tests and the calculated Zn^{2+} transfer number based on (a) the bare Zn and (b) COP@Zn anodes.

Note: The Zn^{2+} transference number (t) was calculated by the following equation:

$$t_{Zn^{2+}} = \frac{I_s(\Delta V - I_0 R_0)}{I_0(\Delta V - I_s R_s)} \#$$

Where ΔV (10 mV) is the bias voltage, R_0 and R_s are the initial and steady-state charge transfer resistances of the electrode, and I_0 and I_s are the initial and steady-state current, respectively.

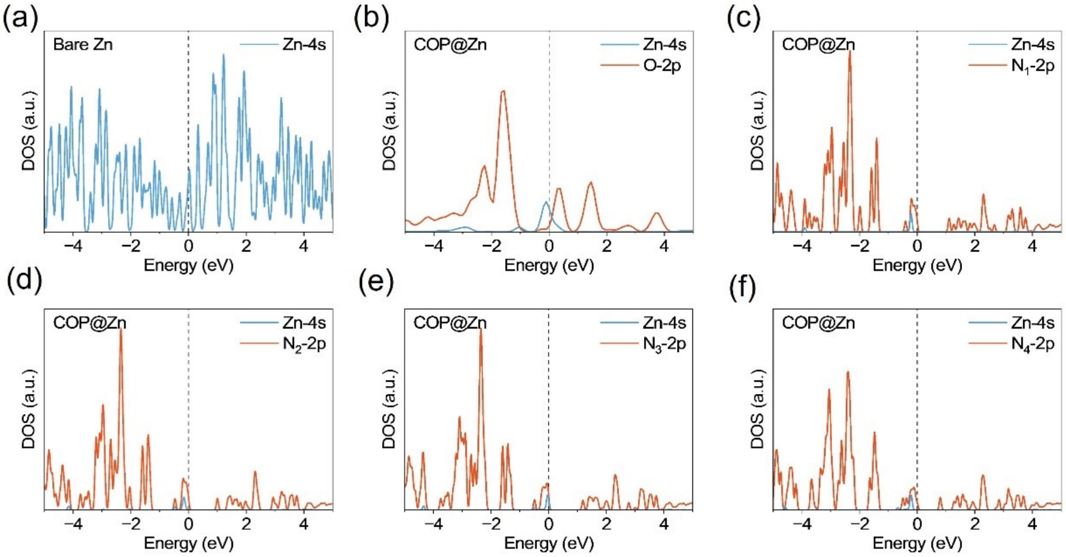

Figure S23 The PDOS of Zn 4s and O/N 2p orbital of COP in COP@Zn system.

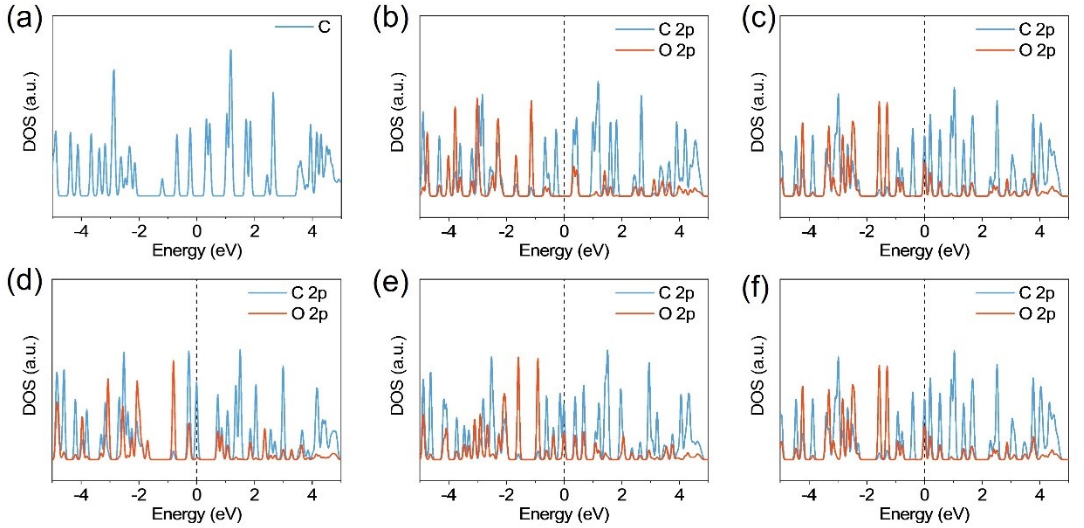

Figure S24. The PDOS of C 2p of COP and O 2p orbital of H_2O in COP@Zn system.

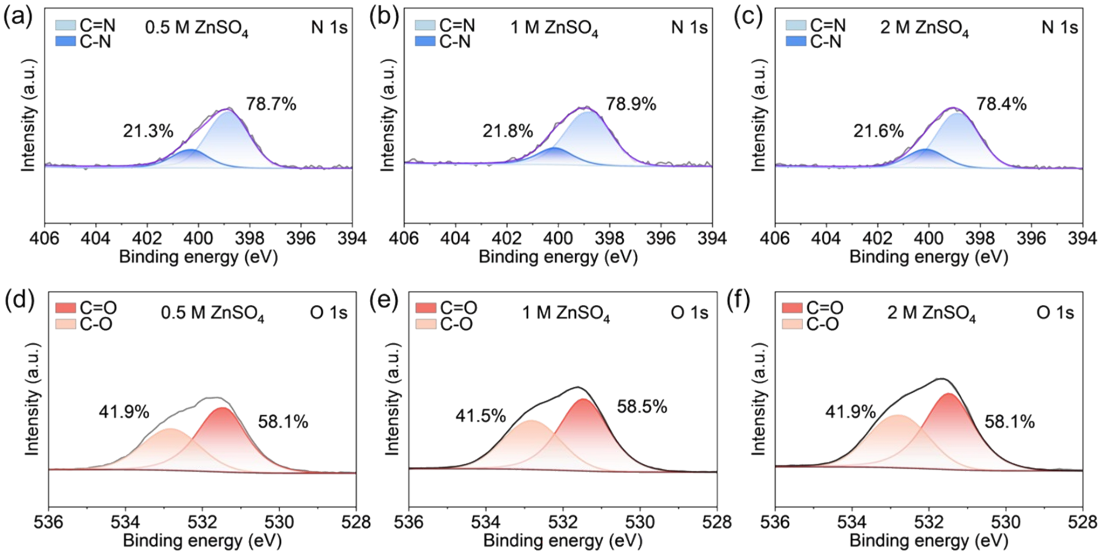

Figure S25. XPS spectra of (a-c) N 1s and (d-f) O 1s of the COP@Zn after soaking in different concentrations of the $ZnSO_4$ electrolytes.

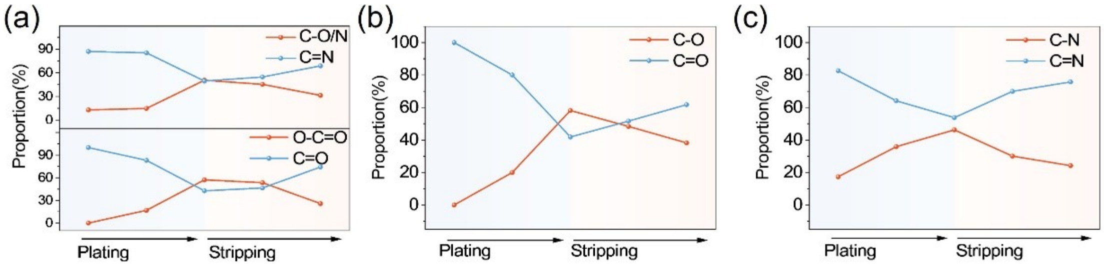

Figure S26. The content evolution of different chemical bonds during Zn^{2+} planting and stripping process.

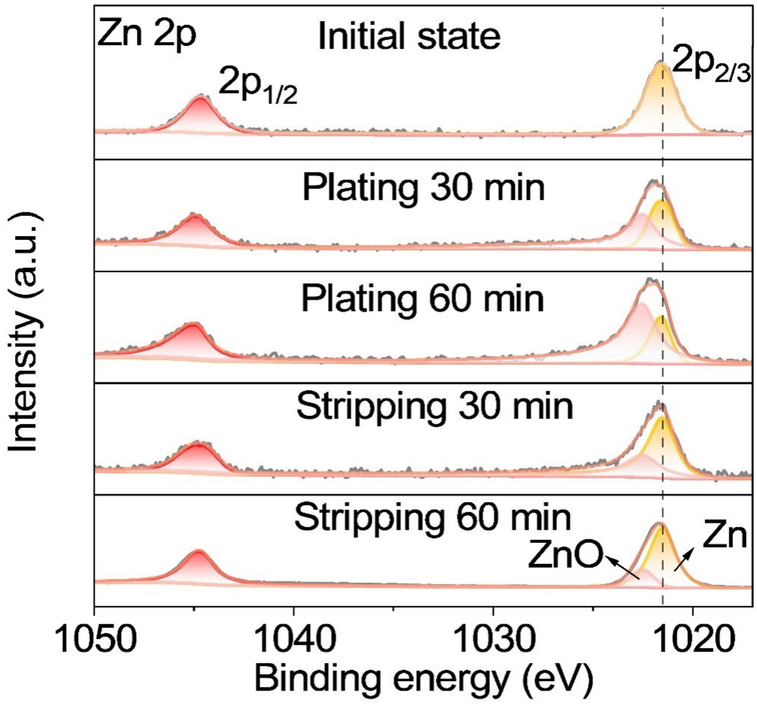

Figure S27. Ex situ XPS spectra of Zn 2p during Zn plating and stripping process.

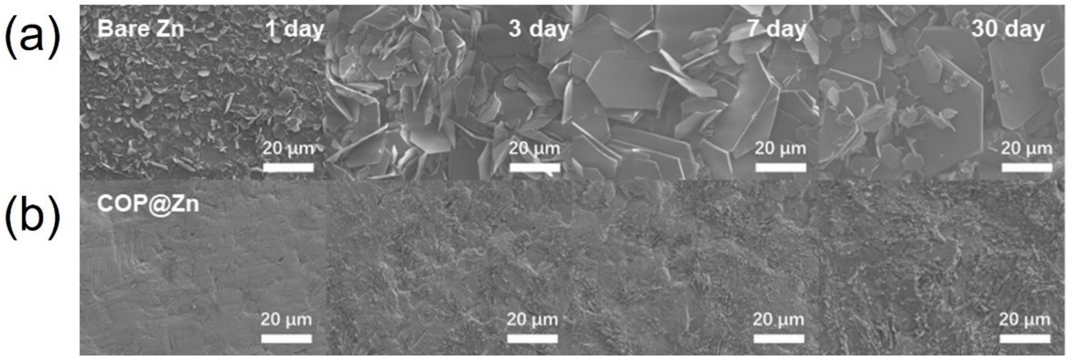

Figure S28. SEM images of the bare Zn and COP@Zn surfaces after immersing in the electrolyte at different days.

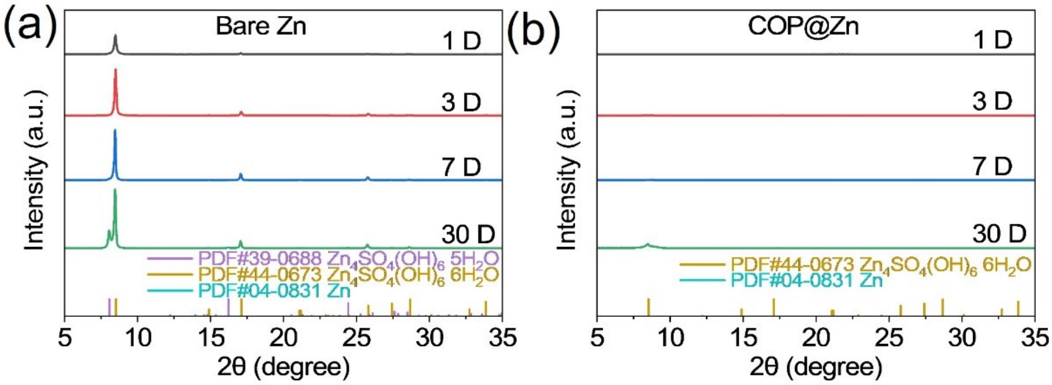

Figure S29. XRD patterns of the (a) bare Zn and (b) COP@Zn after immersing the electrolyte at different days.

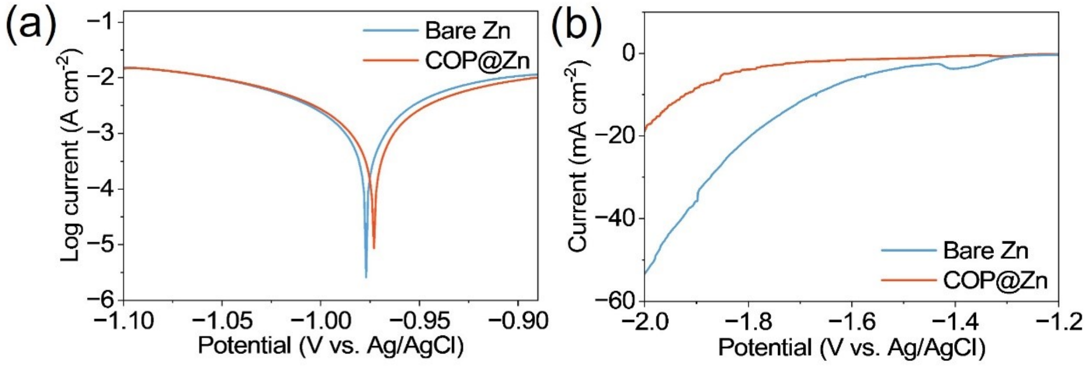

Figure S30. (a) Tafel curves of the bare Zn and COP@Zn at 2 mV s^{-1}. (b) LSV curves of the bare and COP@Zn anodes at 5 mV s^{-1}.

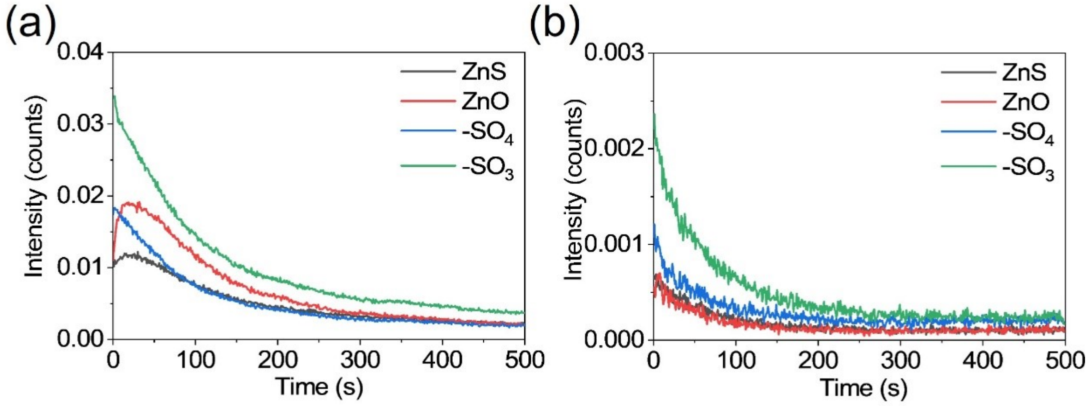

Figure S31. Depth profiling TOF-SIMS analysis of the (a) Zn and (b) COP@Zn anodes.

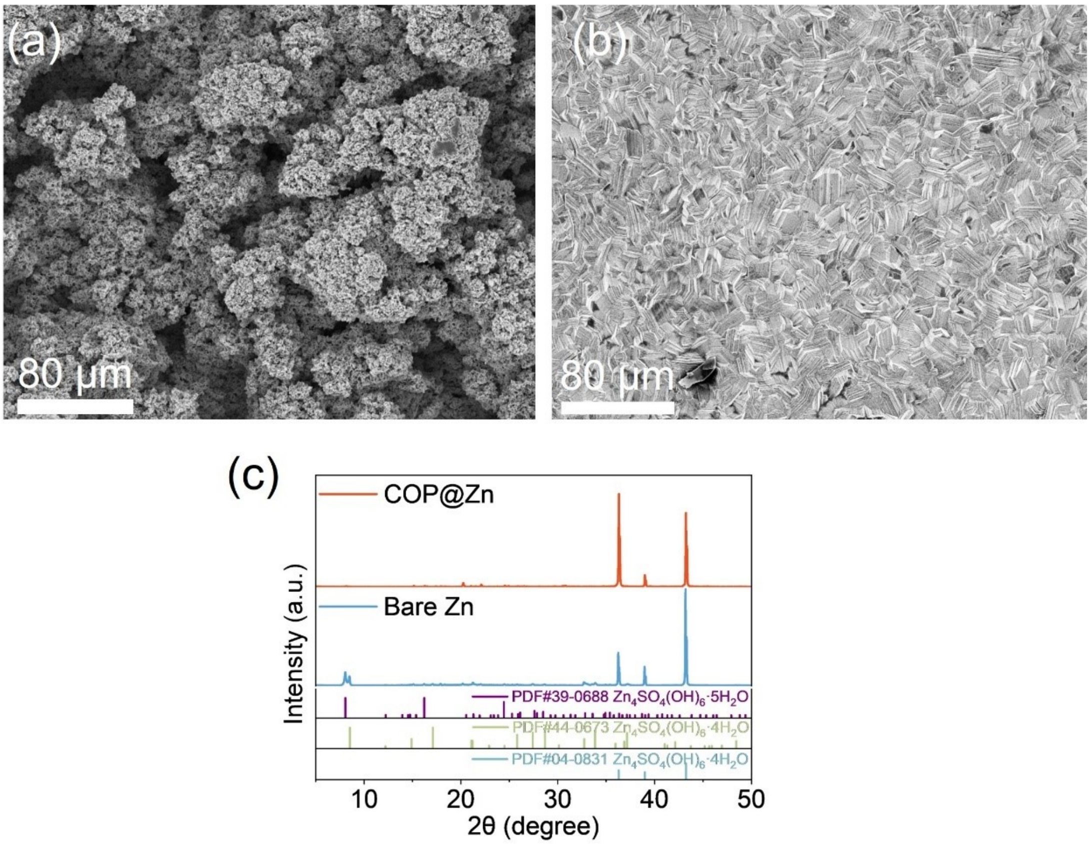

Figure S32. SEM images of the Zn surfaces after the in situ optical microscope measurement on (a) the bare Zn and (b) the COP@Zn anode, and (c) the corresponding XRD patterns.

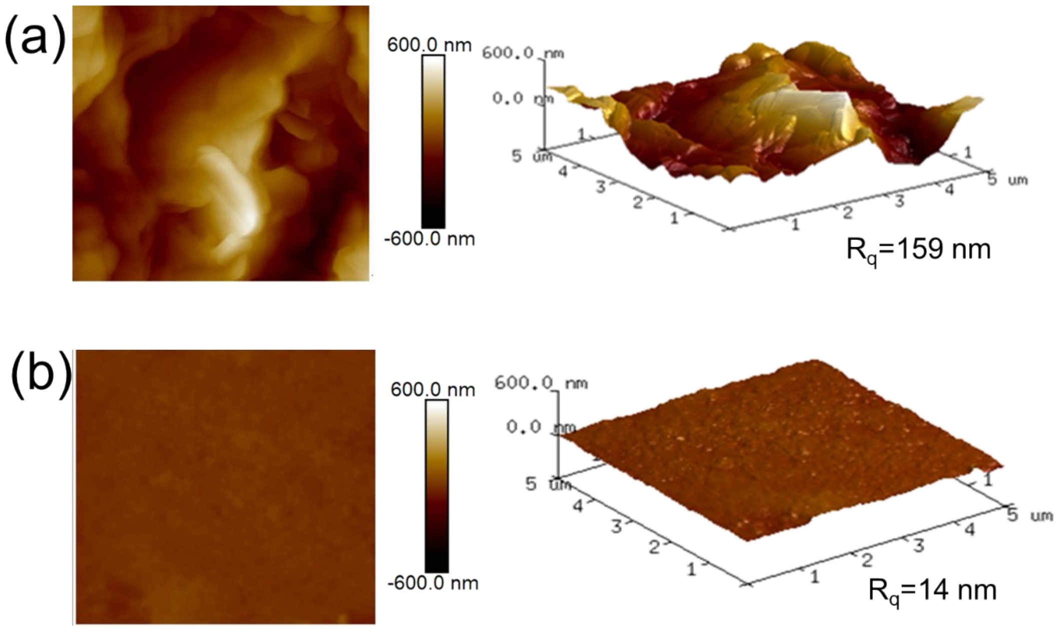

Figure S33. The 2D and 3D images of AFM of recycled Zn anode and COP@Zn anode.

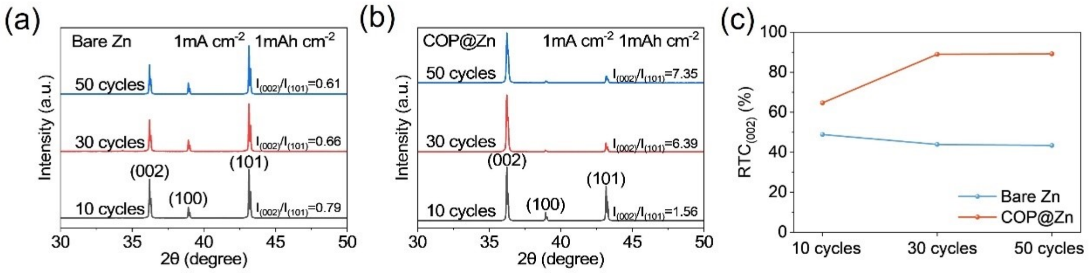

Figure S34. XRD patterns of the (a) bare Zn and (b) COF@Zn anodes after different cycles; and (c) the corresponding RTC analysis of (002) crystalline orientation.

Note: The RTC values of the Zn anode after different cycles have been provided in Figure S35. It is clearly that the COP@Zn anode shows the higher RTC value for the (002) crystal facet compared to the bare Zn anode, also confirming the preferred (002) crystal growth for Zn deposition on the COP@Zn surface.

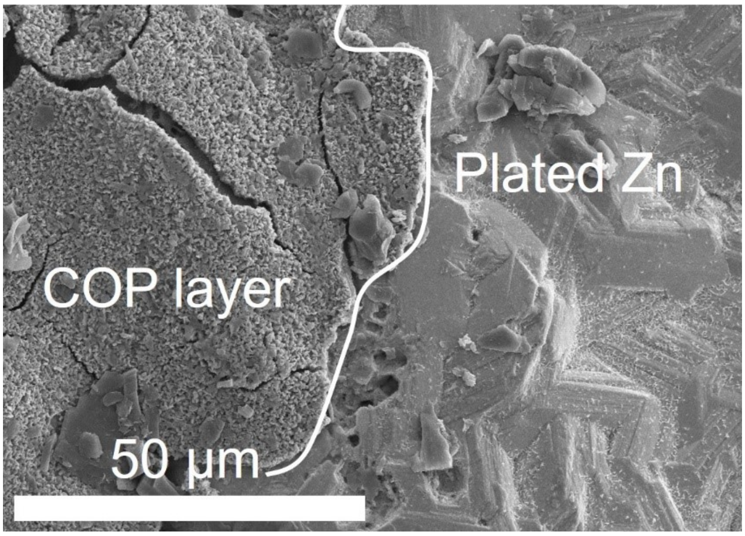

Figure S35. SEM image of the Zn-plated COP@Zn surface with partially stripped COP layer.

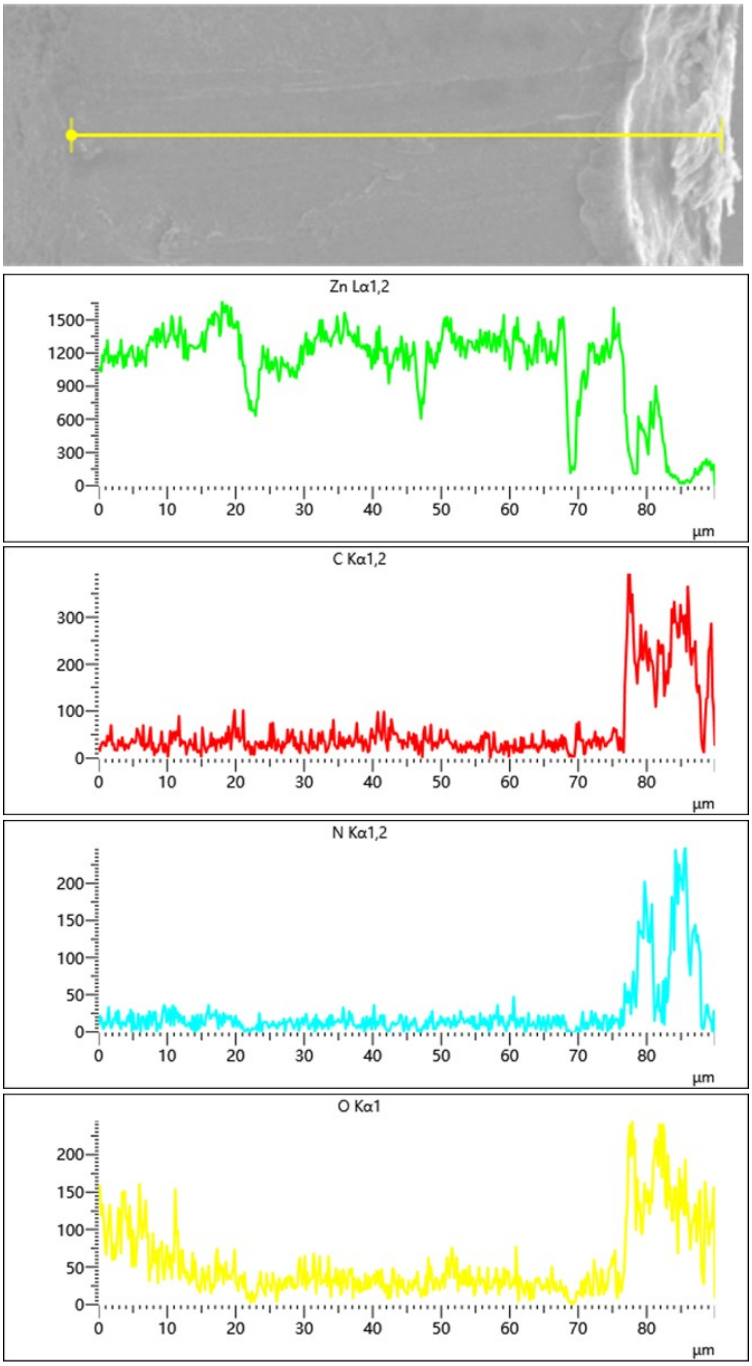

Figure S36. The distribution of the element across the COF@Zn surface after cycling.

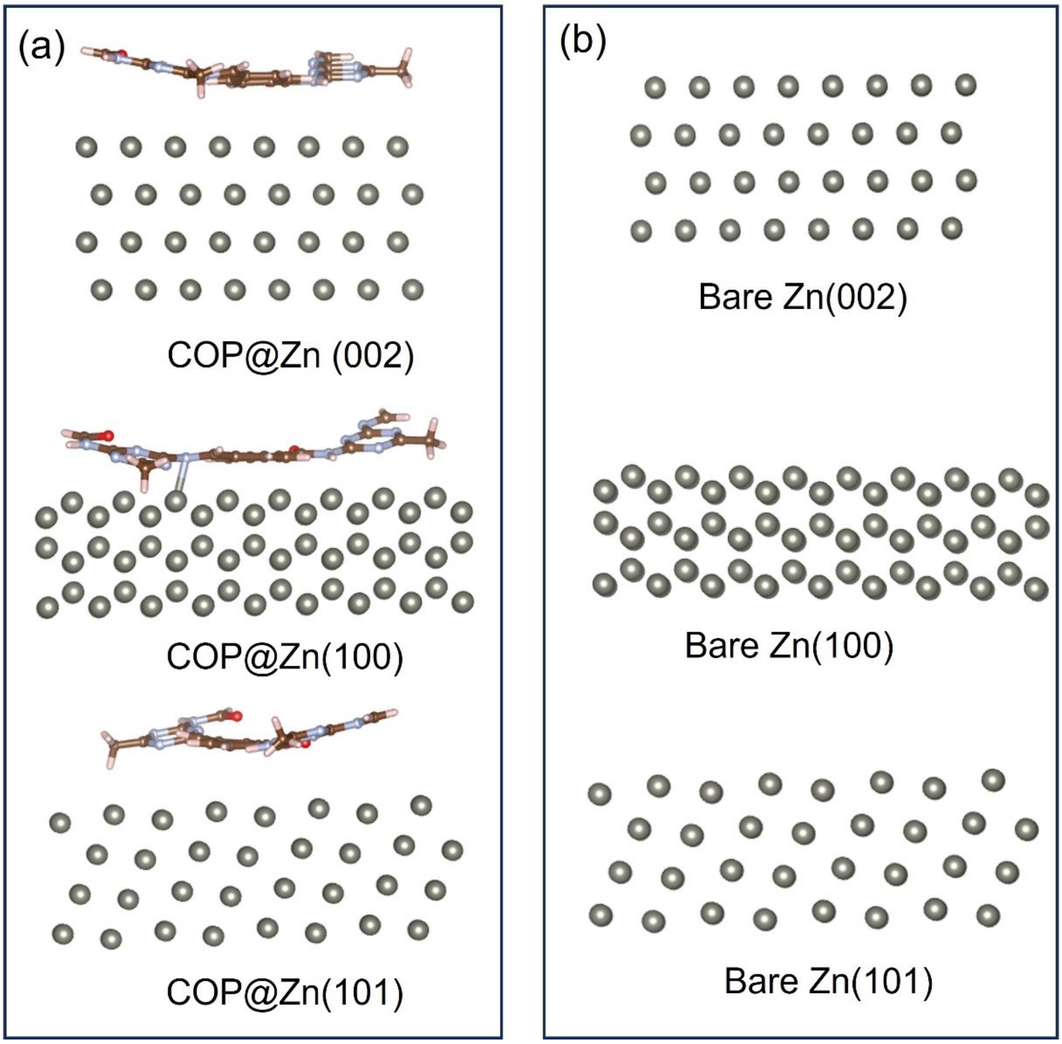

Figure S37. (a) Calculations models of COPs adsorbed on Zn (002), Zn (100) and Zn (101), compared with (b) bare Zn (002), Zn (100) and Zn (101).

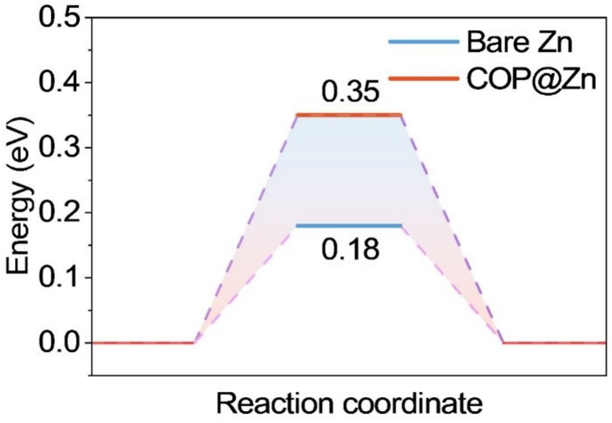

Figure S38. The energy barrier for Zn migration on the bare Zn and COP@Zn surfaces.

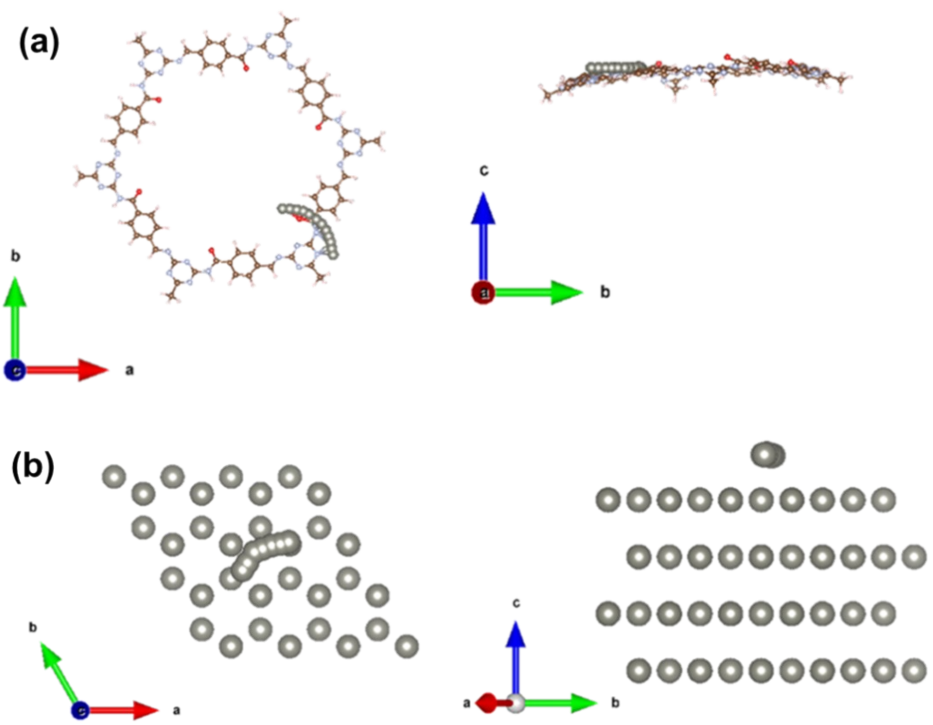

Figure S39. The calculation models for Zn^{2+} migration pathways on the (a) COP@Zn surface and (b) the bare Zn surface.

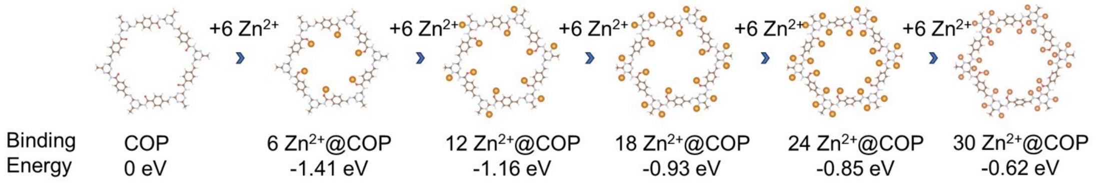

Figure S40. The optimized adsorption configuration of Zn^{2+} on the C=N/O sites of the COP and the corresponding adsorption energy.

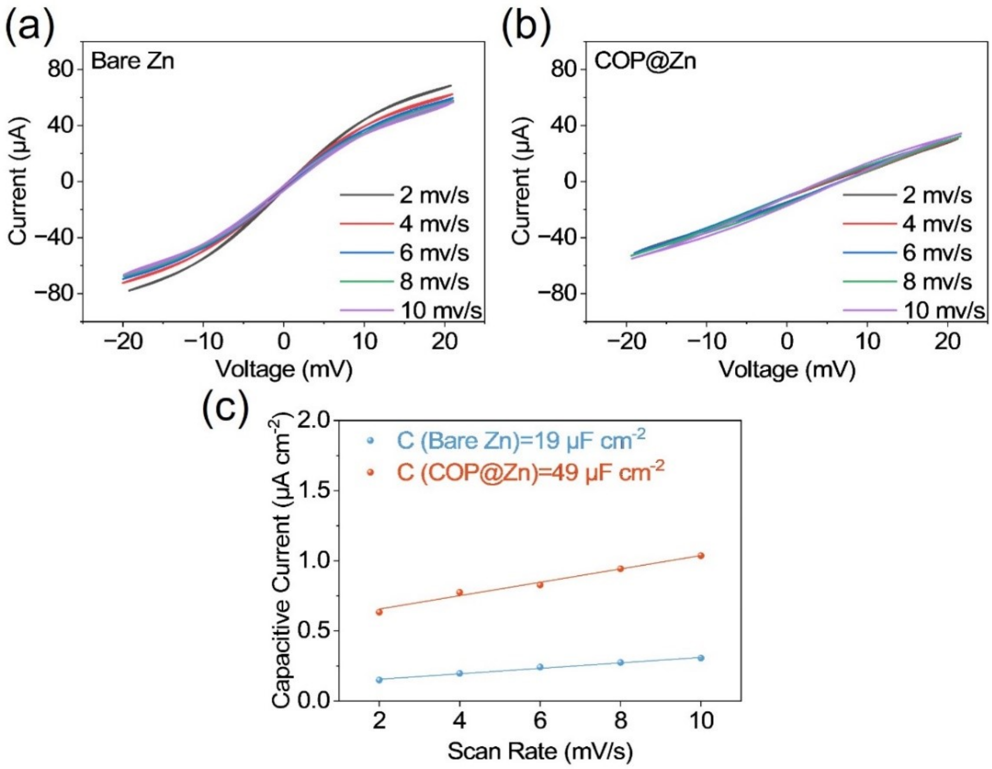

Figure S41. CV curves of the Zn symmetric cells in (a) bare Zn and (b) COP@Zn anode, and (c) the corresponding calculated EDLCs.

Note: The double layer (EDL) capacitance of zinc/zinc symmetric batteries is measured by cyclic voltammetry (CV) tests at different sweep rates. The double layer capacitance (C, mF cm^{-2}) with respect to Zn/Zn^{2+} is calculated using the formula C=i/v at a potential of 0 V, where i and v are the corresponding current density and sweep rate, respectively.

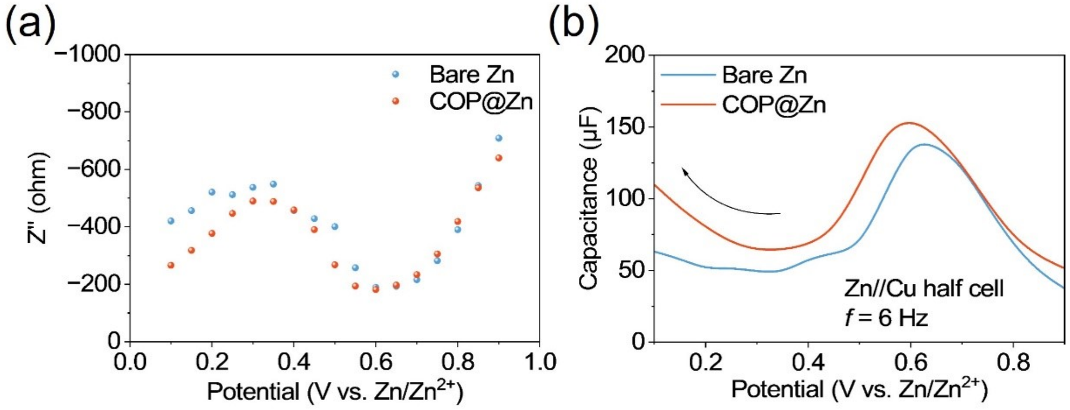

Figure S42. (a) The Z'' data of bare Zn and COP@Zn anodes at different potentials. (b) The differential capacitance curve of bare Zn and COP@Zn anodes in 2 M $ZnSO_4$.

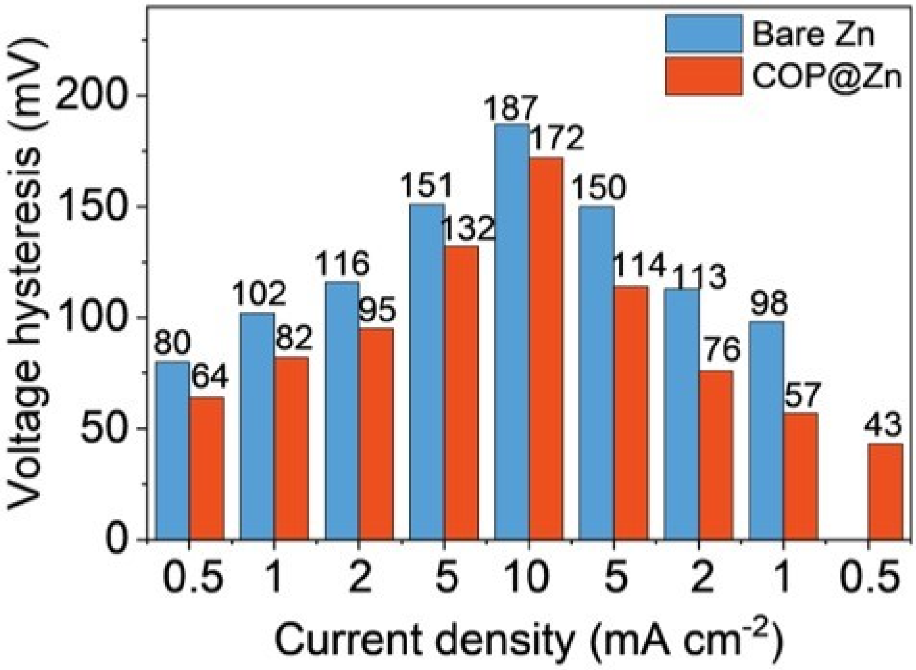

Figure S43. The voltage hysteresis of the bare Zn and COP@Zn-based symmetric cells at different current densities. Note: the voltage hysteresis for the bare Zn-based symmetric cell when it returns back to 0.5 mA cm^{-2} is invalid due to its broken down.

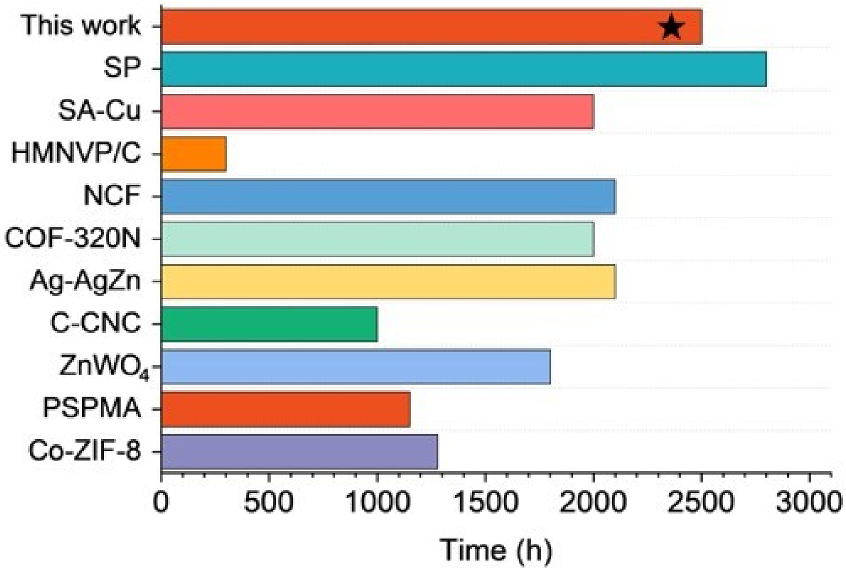

Figure S44. The comparison of the cycling performance in symmetric cell with ever-reported works.

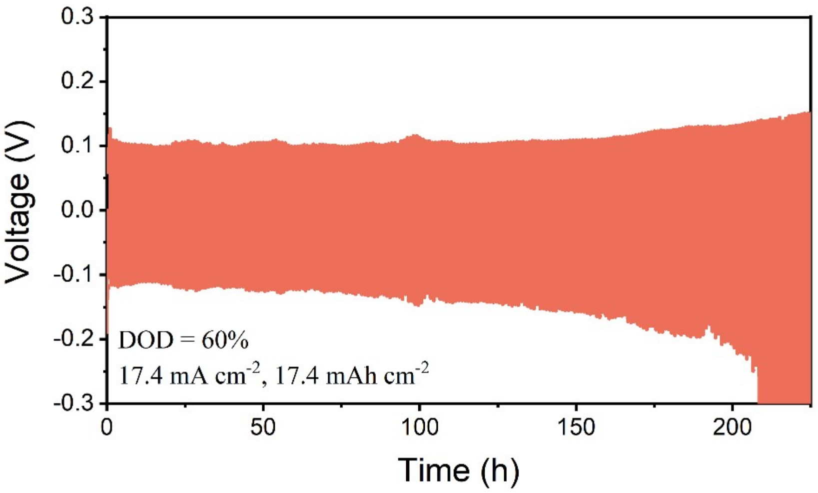

Figure S45. The cycling stability of the COP@Zn based symmetric cell under a DOD at 60% using the 50 μm-thick Zn foils.

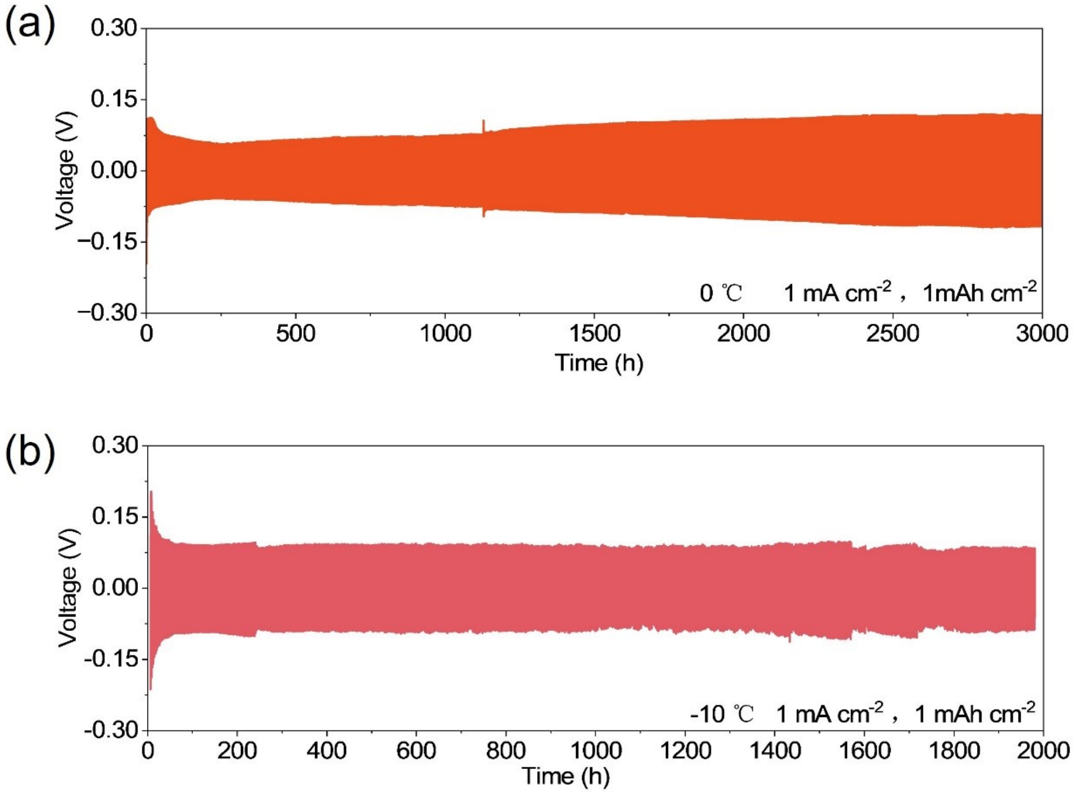

Figure S46. Cycling stability of the Zn//Zn symmetric cell at 1 mA cm^{-2}, 1 mAh cm^{-2} under 0°C and −10 °C.

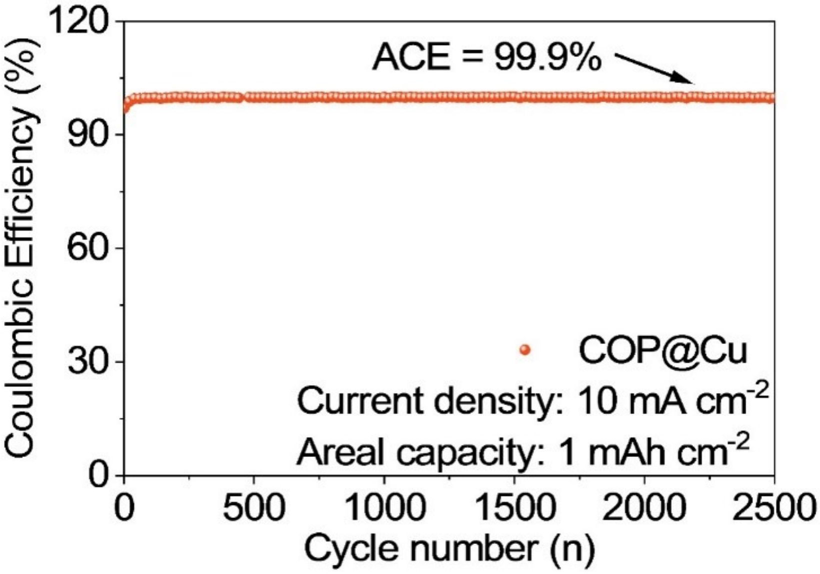

Figure S47. The Coulombic efficiency of the Zn//Cu asymmetric cell at 10 mA cm^{-2}, 1 mAh cm^{-2}.

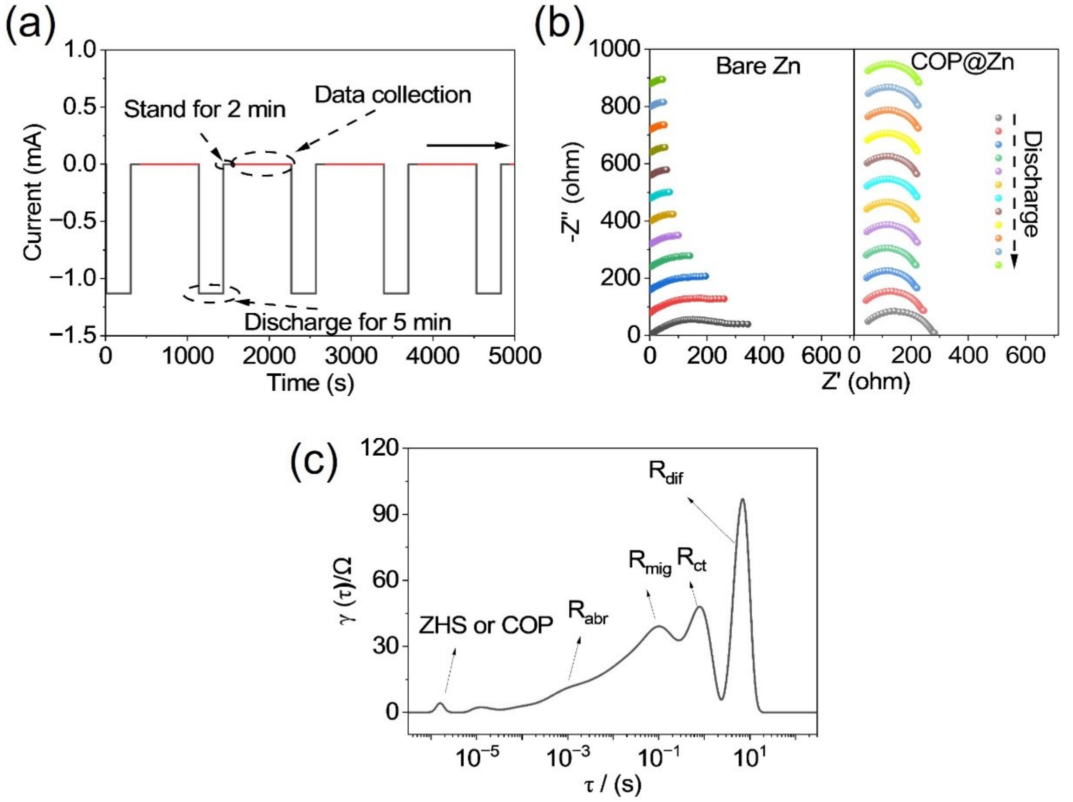

Figure S48. (a) Charging and discharging schematic for in situ EIS measurement. (b) In situ EIS curves of the Zn//Zn cells. (c) The DRT model of in situ EIS. Notably, the first Nyquist plot (Figure S49b) for the EIS data collection was conducted after 5 mins Zn plating rather than under the open circuit.

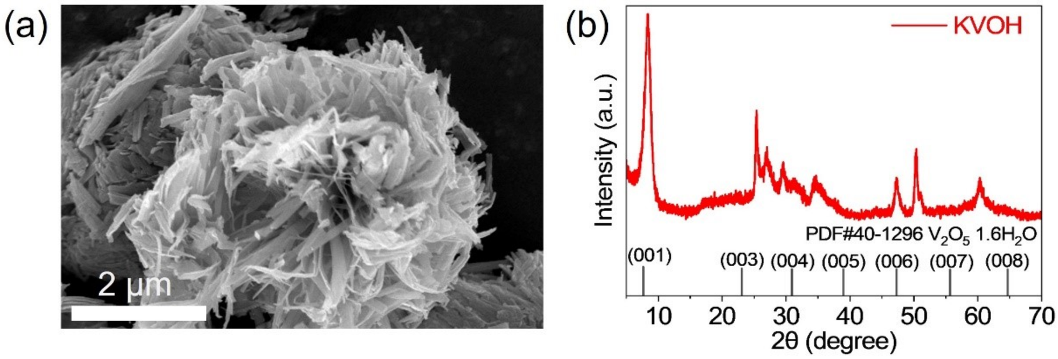

Figure S49. (a) SEM image and (b) XRD pattern of the KVOH.

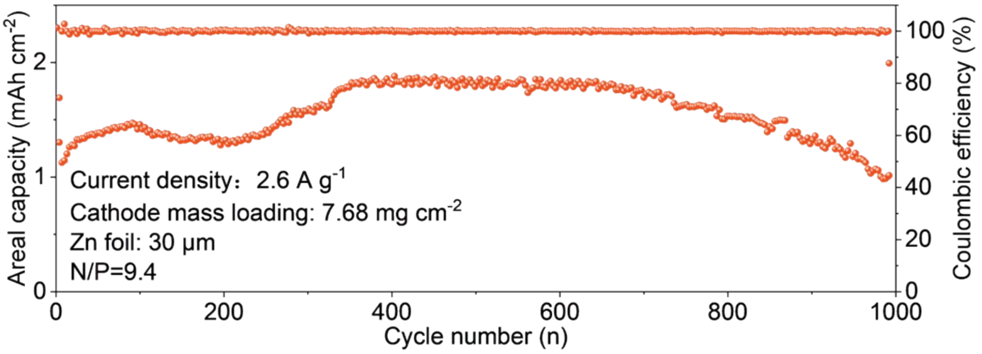

Figure S50. Specific capacity of the full cell with high KVO loading of 7.68 mg cm^{-2} and high current density of 2.6 A g^{-1} with a N/P ratio of 9.4.

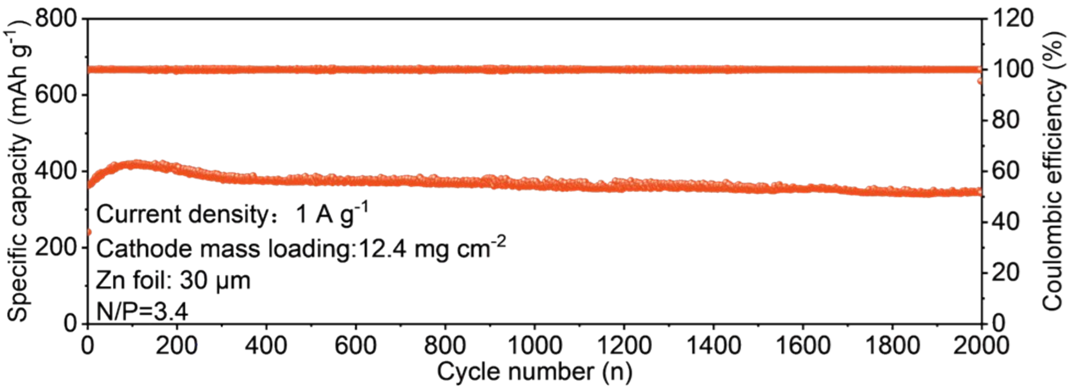

Figure S51. Cycling performance of the full cell with a KVO mass loading of 12.4 mg cm^{-2} under a low N/P ratio of 3.4.

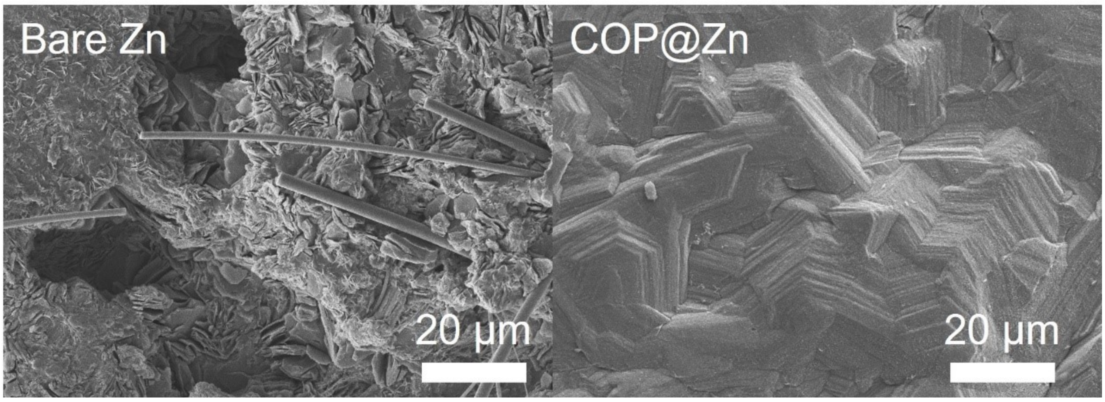

Figure S52. The SEM images of the bare Zn anode and COP@Zn anode after 500 cycles at 10 A g^{-1}.

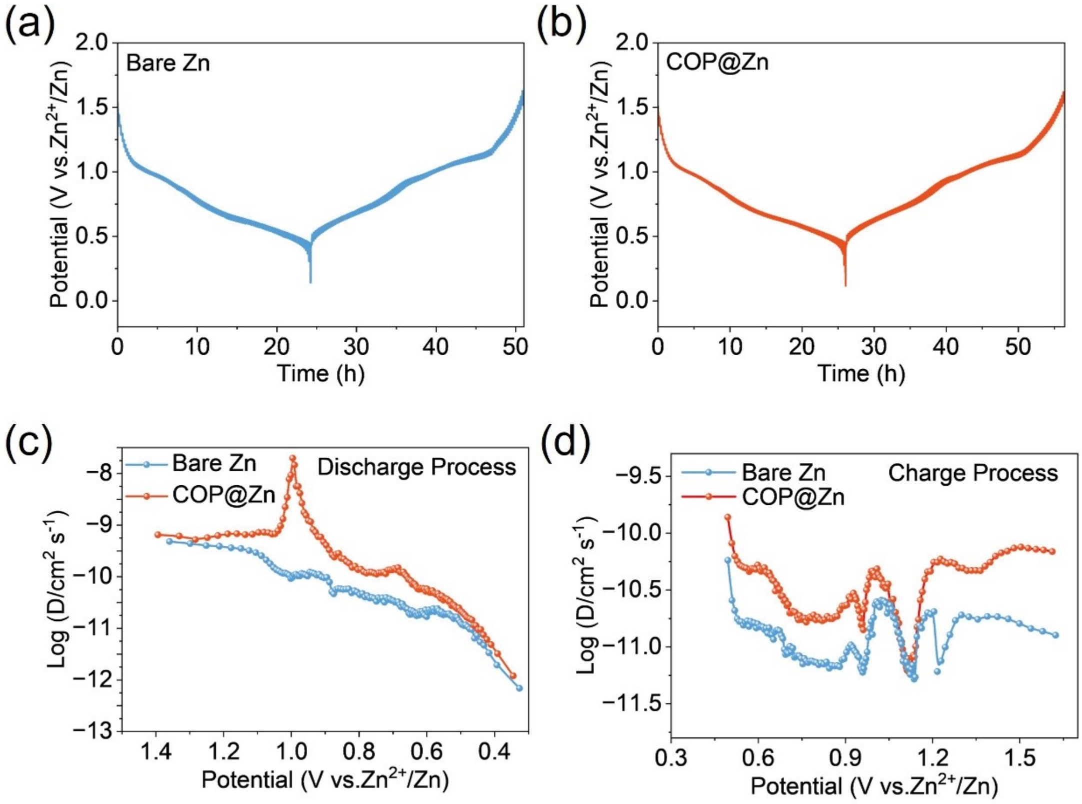

Figure S53. The GITT profiles of (a) bare Zn-based and (b) COP@Zn based cells. The corresponding on diffusion coefficients of (c) bare Zn-based and (d) COP@Zn based cells.

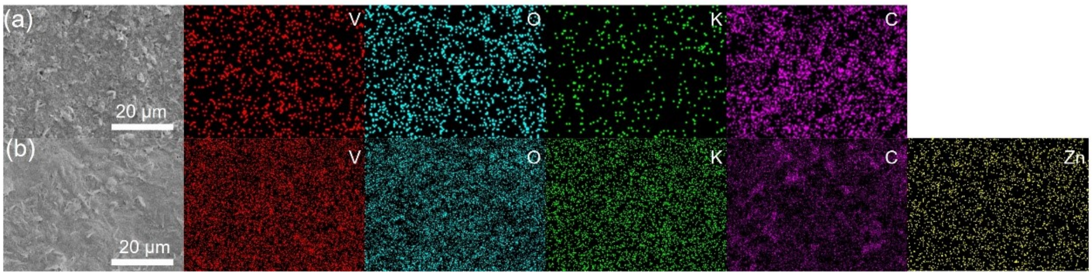

Figure S54. The SEM image and corresponding EDS mapping of KVO cathode before and after cycling.

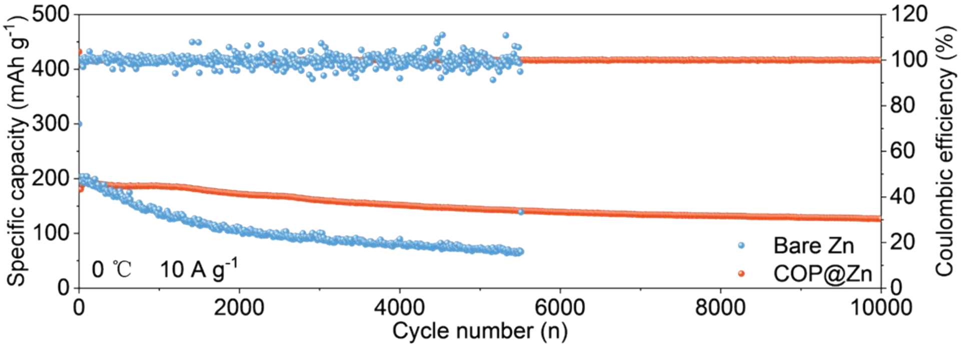

Figure S55. Cycling performance of the full cell at 0 ℃.

Supplementary Table 1. The number of electrons of different atoms at the adsorption site.

	C of C=O	O of C=O	C of C=N	N of C=N
COP	3.65	6.61	3.88	5.78
COP@$[Zn(H_2O)_6]^{2+}$	3.79	6.79	4.01	5.84
Electron change numbers	0.14	0.18	0.13	0.16

Supplementary Table 2. Adsorption energies of Zn atom on different sites.

Binding sites	Binding energy (eV)
Zn - Zn	-0.05
Zn - H2O	-0.31
Zn - O	-2.43
Zn - N_1	-1.83
Zn - N_2	-1.93
Zn - N_3	-2.13
Zn - N_4	-1.23

Supplementary Table 3. The percentage of peak area occupied by SSIP and CIP during in-situ FTIR deposition

Plating time (min)	SSIP (Bare Zn)	CIP (Bare Zn)	SSIP (COP@Zn)	CIP (COP@Zn)
10	54.8%	45.8%	6.2%	93.8%
20	59.7%	40.3%	22.3%	77.7%
30	67.3%	32.7%	30.6%	69.4%
40	69.1%	30.9%	36.8%	63.2%
50	71.4%	28.6%	51.9%	48.1%
60	77.4%	22.6%	58.3%	41.7%

Supplementary Table 4. The proportion of different peak areas of COP@Zn in situ Raman during sedimentation

Plating time (min)	SSIP	CIP	ν_{HOH-OH_2}	$\nu_{HOH-OSO_3^{2-}}$
0	63.2%	36.8%	33.5%	66.5%
12	49.8%	50.2%	33.3%	66.7%
24	49.6%	50.4%	29.5%	70.5%
36	48.4%	51.6%	28.2%	71.8%
48	46.6%	53.4%	26.2%	73.8%
60	45.5%	54.5%	24.1%	75.9%

Supplementary Table 5. The proportion of different peak areas of bare Zn in situ Raman during sedimentation

Plating time (min)	SSIP	CIP	ν_{HOH-OH_2}	$\nu_{HOH-OSO_3^{2-}}$
0	69.8%	30.2%	54.9%	45.1%
6	66.0%	34.0%	42.1%	57.9%
12	59.6%	40.4%	49.4%	50.6%

Supplementary Table 6. The Rs, Rct value of the electrode at different temperatures

	Bare Zn		COP@Zn	
Temperature (°C)	Rs (Ω)	Rct (Ω)	Rs (Ω)	Rct (Ω)
10	2.5	2402	2.2	483.4
20	2.0	1463	2	341.4
30	1.9	943.5	1.9	278.9
40	1.7	541.3	2.1	166.4
50	1.6	305.5	2.1	139.4
60	1.4	205.8	2.0	102.2

Supplementary Table 7. C 1s of XPS binding energy and peak assignment for the COP@Zn during Zn plating and stripping process.

C 1s	Position (eV)	Plating 0 min	Plating 30 min	Plating 60 min	Stripping 30 min	Stripping 60 min	Assignment
	284.4	26.67%	35.89%	35.64%	40.63%	41.64%	C=C
	285.4	9.41%	26.91%	16.06%	16.81%	23.94%	C=N
	286.7	3.66%	9.51%	16.57%	13.62%	5.57%	C-O/N
	289.1	60.26%	23.03%	13.58%	13.43%	18.24%	C=O
	291	--	4.67%	18.15%	15.50%	10.61%	O-C=O

Supplementary Table 8. The comparison of the electrochemical performance of the COP@Zn//COP@Zn symmetric cells with the reported works.

Materials	Current density (mA cm^{-2})	Time (h)	Ref.
COP	1	2500	This Work
Co-ZIF-8	1	1280	6
PSPMA	1	1150	7
$ZnWO_4$	1	1800	8
C-CNC	1	1000	9
Ag-AgZn	1	2100	10
COF-320N	1	2000	11
NCF	1	2100	12
HMNVP/C	1	300	13
SA-Cu	1	2000	14
SP	1	2800	15

Supplementary Table 9. The comparison of the electrochemical performance of the COP@Zn anodes with the reported works.

Materials	Current density (A g^{-1})	Maximum capacity (mAh g^{-1})	Cycle number	Ref.
COP	10	280	28000	This Work
SITL	0.2	250	100	16
ZrO_2	1	290	250	17
P2VP	1	270	500	18
PDPTT	5	300	1000	19
Chelex-In	5	285	1300	20
SUC1	4	170	4000	21
p-DB@CF	5	225	25000	22
ZAP	2	140	2000	23
PEO	10	190	3000	24
PAN	10	300	1500	25
ZnVOx	10	320	7000	26
SZ	15	190	10000	27
DP	10	124	15000	28
ALK	20	270	20000	29
GHNs	10	100	1800	30
Vd	5	140	30000	31

Reference:

1. Y. Lu, C. Z. Zhao, J. Q. Huang, Q. Zhang, *Joule* **2022**, *6* (6), 1172-1198.
2. G. Kresse, J. Furthmüller, *Comput. Mater. Sci.* **1996**, *6* (1), 15-50.
3. G. Kresse, J. Furthmüller, *Phys Rev B.* **1996**, *54* (16), 11169-11186.
4. J. P. Perdew, K. Burke, M. Ernzerhof, *Phys. Rev. Lett.* **1996**, *77* (18), 3865-3868.
5. P. E. Blöchl, *Phys Rev B.* **1994**, *50* (24), 17953-17979.
6. Z. J, Jiang, Z. J. Du, R. Pan, F. H. Cui, G. J. Zhang, S. Y. Lei, G. J. He, K. B. Yin, L. T. Sun, *Adv. Energy Mater.* **2024**, *14*, 2402150.
7. H. Y. Liu, Q. Ye, D. Lei, Z. D. Hou, W. Hua, Y. Huyan, N. Li, C. G. Wei, F. Y. Kang, J. G. Wang, *Energy Environ. Sci.* **2023**, *16*, 1610.
8. J. Cao, H. Y. Wu, D. D. Zhang, D. Luo, L. L. Zhang, X. L. Yang, J. Q. Qin, G. J. He, *Angew. Chem. Int. Ed.* **2024**, *63*, e202319661.
9. X. Z. Cai, W. L. Wu, B. Y. Zhang, W. L. Cai, C. H. Lu, R. Xiong, J. Q. Zhao, J. Zhou, *Energy Environ. Sci.* **2025**, *18*, 3313.
10. J. X. Zheng, X. Liu, Y. G. Zheng, A. N. Gandi, X. X. Kuai, Z. C. Wang, Y. P. Zhu, Z. C. Zhuang, H. F. Liang, *Nano Lett.* **2023**, *23*, 6156−6163.
11. S. D. Zhang, J. S. Chen, W. G. Chen, Y. W. Su, Q. Z. Gou, R. D. Yuan, Z. Y. Wang, K. X. Wang, W. T. Zhang, X. Q. Hu, Z. X. Zhang, P. Y. Wang, F. Wan, J. Liu, B. B. Li, Y. F. Wang, G. P. Zheng, M. Li, J. Y. Sun, *Angew. Chem. Int. Ed.* **2025**, *64*, e202424184.
12. Y. F. Liu, X. T. Zhang, S. M. Shaaban, Z. C. Li, D. A. Alshammari, X. Y. Xu, Y. Tang, Z. M. El-Bahy, B. G. Lu, Y. Y. Liu, J. Zhou, *Adv. Energy Mater.* **2025**, 2500962.
13. J. Z. Hong, B. N. Zhu, M. X. Song, X. S. Wang, B. S. Gao, Y. N. Liu, X. X. Huang, *Adv. Funct. Mater.* **2025**, 2424731.
14. L. S. Han, Y. M. Guo, F. H. Ning, X. Y. Liu, J. Yi, Q. Luo, B. h. Qu, J. L. Yue, Y. F. Lu, Q. Li, *Adv. Mater.* **2024**, *36*, 2308086.
15. Z. Y. Liu, S. L. Chen, Z. H. Shi, P. Qiu, K. He, Q. Q Lu, M. H. Yu, T. X. Liu, *Adv. Energy Mater.* **2025**, 2502010.
16. Y. H. Lee, Y. Jeoun, J. H. Kim, J. Shim, K. S. Ahn, S. H. Yu, Y. E. Sung, *Adv. Funct. Mater.* **2024**, *34* (10), 2310884.
17. B. Wei, J. Zheng, Abhishek, X. Liu, J. Wu, Z. Qi, Z. Hou, R. Wang, J. Ma, A. N. Gandi, Z. Wang, H. Liang, *Adv. Energy Mater.* **2024**, *14* (24), 2401018.

18. X. Cai, W. Tian, Z. Zhang, Y. Sun, L. Yang, H. Mu, C. Lian, H. Qiu, *Adv. Mater.* **2024**, *36* (3), 2307727.
19. M. Chen, X. Guo, X. Jiang, B. Farhadi, X. Guo, Y. Zhu, H. Zhang, S. Liu, *Angew. Chem. Int. Ed.* **2024**, *63* (39), e202410011.
20. M. Zhang, S. Li, R. Tang, C. Sun, J. Yang, G. Chen, Y. Kang, Z. Lv, Z. Wen, C. C. Li, J. Zhao, Y. Yang, *Angew. Chem. Int. Ed.* **2024**, *63* (29), e202405593.
21. H. Dou, X. Wu, M. Xu, R. Feng, Q. Ma, D. Luo, K. Zong, X. Wang, Z. Chen, *Angew. Chem. Int. Ed.* **2024**, *63* (21), e202401974.
22. Z. Song, L. Miao, H. Duan, L. Ruhlmann, Y. Lv, D. Zhu, L. Li, L. Gan, M. Liu, *Angew. Chem. Int. Ed.* **2022**, *61* (35), e202208821.
23. N. Yang, Y. Gao, F. Bu, Q. Cao, J. Yang, J. Cui, Y. Wang, J. Chen, X. Liu, C. Guan, *Adv. Mater.* **2024**, *36* (26), 2312934.
24. M. Wu, C. Shi, J. Yang, Y. Zong, Y. Chen, Z. Ren, Y. Zhao, Z. Li, W. Zhang, L. Wang, X. Huang, W. Wen, X. Li, X. Ning, X. Ren, D. Zhu, *Adv. Mater.* **2024**, *36* (23), 2310434.
25. Y. Fang, X. Xie, B. Zhang, Y. Chai, B. Lu, M. Liu, J. Zhou, S. Liang, *Adv. Funct. Mater.* **2022**, *32* (14), 2109671.
26. Y. Liu, X. Wu, *Nano Energy* **2024**, *127*, 109809.
27. Y. Qin, X. Wang, *Angew. Chem. Int. Ed.* **2024**, *63* (2), e202315464.
28. M. Zhang, X. Zhang, Q. Dong, S. Zhang, Z. Xu, Z. Hou, Y. Qian, *Adv. Funct. Mater.* **2023**, *33* (31), 2213187.
29. C. Chen, T. Wang, X. Zhao, A. Wu, S. Li, N. Zhang, X. Qu, L. Jiao, Y. Liu, *Adv. Funct. Mater.* **2024**, *34* (9), 2308508.
30. Y. Cui, W. Chen, W. Xin, H. Ling, Y. Hu, Z. Zhang, X. He, Y. Zhao, X. Y. Kong, L. Wen, L. Jiang, *Adv. Mater.* **2024**, *36* (6), 2308639.
31. K. Zhu, S. Wei, H. Shou, F. Shen, S. Chen, P. Zhang, C. Wang, Y. Cao, X. Guo, M. Luo, H. Zhang, B. Ye, X. Wu, L. He, L. Song, *Nat. Commun.* **2021**, *12* (1), 6878.